INTERNATIONAL JOURNAL FOR NUMERICAL METHODS IN FLUIDS
*Int. J. Numer. Meth. Fluids* 2002; **39**:41–73 (DOI: 10.1002/fld.279)

# Comparison of spectral and finite element methods applied to the study of the core-annular flow in an undulating tube

Charalampos Kouris[1], Yannis Dimakopoulos[1], Georgios Georgiou[2] and John Tsamopoulos[1,*,†]

[1]*Laboratory of Computational Fluid Dynamics, Department of Chemical Engineering, University of Patras, Patras 26500, Greece*
[2]*Department of Mathematics and Statistics, University of Cyprus, P.O. Box 20537, 1678 Nicosia, Cyprus*

SUMMARY

A Galerkin/finite element and a pseudo-spectral method, in conjunction with the primitive (velocity-pressure) and streamfunction-vorticity formulations, are tested for solving the two-phase flow in a tube, which has a periodically varying, circular cross section. Two immiscible, incompressible, Newtonian fluids are arranged so that one of them is around the axis of the tube (core fluid) and the other one surrounds it (annular fluid). The physical and flow parameters are such that the interface between the two fluids remains continuous and single-valued. This arrangement is usually referred to as Core-Annular flow. A non-orthogonal mapping is used to transform the uneven tube shape and the unknown, time dependent interface to fixed, cylindrical surfaces. With both methods and formulations, steady states are calculated first using the Newton–Raphson method. The most dangerous eigenvalues of the related linear stability problem are calculated using the Arnoldi method, and dynamic simulations are carried out using the implicit Euler method. It is shown that with a smooth tube shape the pseudo-spectral method exhibits exponential convergence, whereas the finite element method exhibits algebraic convergence, albeit of higher order than expected from the relevant theory. Thus the former method, especially when coupled with the streamfunction-vorticity formulation, is much more efficient. The finite element method becomes more advantageous when the tube shape contains a cusp, in which case the convergence rate of the pseudo-spectral method deteriorates exhibiting algebraic convergence with the number of the axial spectral modes, whereas the convergence rate of the finite element method remains unaffected. Copyright © 2002 John Wiley & Sons, Ltd.

KEY WORDS: two-phase flow; undulating tube; core-annular flow; pseudo-spectral method; finite element method

## 1. INTRODUCTION

A number of technologically important applications are known in which two immiscible fluids flow concurrently inside a duct with one of them occupying the core of the duct

* Correspondence to: J. Tsamopoulos, Laboratory of Computational Fluid Dynamics, Department of Chemical Engineering, University of Patras, Patras 26500, Greece.
† E-mail: tsamo@chemeng.upatras.gr

*Received November 2000*
*Revised May 2001*

Copyright © 2002 John Wiley & Sons, Ltd.

and the other one the space between the fluid in the core and the surrounding solid wall. In several of these applications, the flow is rather slow, and the corresponding Reynolds number is of the order of unity. In a first such example, hydrogen and hydrocarbons flow through millimeter-scale, tortuous passages created by catalytic particles stacked together to promote reforming oil and its byproducts in certain trickle-bed reactors. It has been conjectured that in this process heavy oil wets the catalytic particles and hydrogen has to diffuse through it in order to reach the particles where reaction takes place. It is well known that the different flow regimes affect greatly the reactor parameters, namely pressure drop, heat and mass transfer coefficients, reaction rate and liquid holdup. Therefore, the prediction of the onset of these flow regimes is critical in reactor design and operation [1]. To this end, they have been studied extensively both experimentally and theoretically using macroscopic or microscopic models of two-phase flow [2]. Similarly, two fluids flow concurrently through corrugated and narrow passages in processes aimed at recovering oil from sedimentary rocks by injecting primarily water or steam. Inevitably, the displacing fluid follows the path of minimum resistance, i.e., away from solid surfaces and, usually, it does not remove the part of the oil that adheres to corners and crevices in the rock.

A popular approximation of the tortuous paths in a packed bed is a conduit of circular cross section, the radius of which varies sinusoidally with the axial distance. This is the so-called periodically constricted tube. Although this single tube geometry cannot describe latitudinal dispersion in the bed or exchange of fluids between nearby conduits, it simulates the converging–diverging character of the flow in an actual packed-bed, which is important, and cannot be described by a straight tube. This model has been used extensively for simulating the single-phase flow of Newtonian [3, 4] and non-Newtonian fluids [5]. However, studies with two-phase flow are very limited. Very recently, Kouris and Tsamopoulos [6, 7] have studied the linear stability of the steady, two-phase flow with and without employing the lubrication approximation, respectively.

On the other hand, the linear and nonlinear theory for two-phase flow is well developed for flows in straight tubes, where capillarity, inertia and viscosity and, secondarily, density stratification are the dominant contributions to the flow stability [8–10]. Unfortunately, the pores between sedimentary rocks and the interstices in packed beds do not provide a pathway of uniform cross section, and it is conceivable that this geometric non-uniformity may induce or modify already possible instability. For this reason, we have undertaken a systematic study of the effect of the conduit's periodically varying cross section on the flow field and its stability. As mentioned above, the most often used periodic shape is the sinusoidally varying tube. However, the space between touching particles does not vary as smoothly. For this reason, we examine here the effect of a more general periodic shape, which depends on a geometric parameter, the limiting values of which reduce it to either the sinusoidal shape or a 'singular' shape. This geometric 'singularity' provides an additional test to the chosen numerical methods of solution.

The numerous physical and flow parameters that arise in this study necessitate the development of an efficient and robust numerical method for performing the required calculations. Here, the steady solution, the most unstable eigenvalues as well as the dynamic response of the core-annular flow in a periodically constricted tube are obtained after solving the governing equations of motion using different formulations (primitive and streamfunction-vorticity) and numerical methods (pseudo-spectral and finite element). A non-orthogonal

Copyright © 2002 John Wiley & Sons, Ltd. 

mapping is employed to transform the time-dependent (physical) domain of each fluid to a fixed (computational) one, where the transformed variables are approximated by polynomial expansions. Because of this mapping, the tube and the interface radii arise explicitly in the bulk equations, thus increasing their complexity. In all formulations and solutions, the flow field and the unknown fluid/fluid interface are calculated simultaneously, accelerating in this way the convergence of the iterative scheme. This requires computing the Jacobian matrix that describes the sensitivity of the residuals of the mass and momentum balances and of the boundary conditions to changes in the field variables and the interface location.

Spectral methods may be viewed as an extreme development of the class of discretization schemes for differential equations known generically as the method of weighted residuals, the key elements of which are the trial functions (the approximating functions) and the test functions (weight functions). The trial functions are used as the basis functions for a truncated series expansion of the solution. The test functions are used to ensure that the differential equation is satisfied as closely as possible by the truncated series expansion. This is achieved by minimizing the residual, i.e., the error in the differential equation produced by using the truncated expansion instead of the exact solution, with respect to a suitable norm. An equivalent requirement is that the residual satisfies a suitable orthogonality condition with respect to each of the test functions. The choice of the trial functions is one of the features, which distinguishes spectral from finite element methods. The trial functions for spectral methods are infinitely differentiable global functions. In the case of the finite element method, the domain is divided into small elements and a low-order trial function is specified in each element. The trial functions are thus local in character, and well suited for handling complex geometries. In the case of the Galerkin/finite element method (FEM) the test functions are the same as the trial ones, while in the case of the pseudo-spectral method the test functions are translated Dirac delta functions centered at special collocation points. The error in approximating a function governed by a differential equation in terms of an infinite sequence of orthogonal trial functions decays faster than any inverse power of the highest retained mode on condition that both the function and all its derivatives are infinitely smooth. This characteristic is usually referred as 'spectral accuracy' of the method. On the other hand, the finite element method exhibits algebraic convergence but its convergence rate is not deteriorated even if the tube shape approaches a singular form and thus, its use becomes much more advantageous compared to the behavior of the spectral method. Here, the spectral expansion of each dependent variable consists of Fourier modes in the axial direction and Chebyshev polynomials in the radial one, while low-order Lagrangian basis functions are used in the case of the FEM.

The remainder of this paper is organized as follows. The governing equations, which depend on eight dimensionless parameters, are presented in Section 2. Next, the necessary transformations using both the streamfunction-vorticity and the primitive formulation are given in Section 3. The numerical method of solution of the model equations in space and time as well as the application of two non-orthogonal body-fitted coordinate transformations using both the pseudo-spectral and the finite element method are described in Sections 4 and 5, respectively. The results are presented in Section 6, where the convergence rate with mesh refinement and the efficiency of each tested numerical scheme are discussed. Finally, conclusions are drawn in Section 7.

Copyright © 2002 John Wiley & Sons, Ltd. 

## 2. GOVERNING EQUATIONS

In what follows, we use the symbol $\hat{}$ to denote dimensional quantities, $\hat{t}$ to denote time and employ cylindrical coordinates $(\hat{r}, \hat{\theta}, \hat{z})$. We consider the core-annular flow (CAF) of two incompressible, immiscible, Newtonian fluids in a pipe of circular cross-section, the radius, $\hat{R}_2$, of which is assumed to vary periodically in the axial direction according to the following equation:

$$\hat{R}_2(\hat{z}) = \frac{\hat{R}_{\max} + \hat{R}_{\min}}{2} - \frac{\hat{R}_{\max} - \hat{R}_{\min}}{2} \cos(\xi(\hat{z})); \quad 0 \leqslant \xi \leqslant 2\pi \tag{1}$$

where the function $\xi(\hat{z})$ is determined by the following implicit expression

$$\xi + \beta \sin(\xi) = 2\pi \frac{\hat{z}}{\hat{L}} \tag{2}$$

According to Equations (1) and (2) the tube radius varies between the values $\hat{R}_{\min}$ and $\hat{R}_{\max}$ within an axial distance $\hat{L}$, and in a way that depends on the parameter $\beta$ as follows. When $\beta = 0$, the variable $\xi$ coincides with $2\pi\hat{z}/\hat{L}$ and, as a result, the tube radius varies sinusoidally with the axial distance generating the widely used undulating tube geometry. On the other hand for $\beta \to 1$ a cusp develops at $\hat{z} = \hat{L}/2$, where the derivative of the radius with respect to $\hat{z}$ develops an infinite jump, generating a 'singular' geometry, used to test and compare further the chosen methods of solution.

The two fluids are layered in such a way so that the first fluid (core fluid) with viscosity and density $(\hat{\mu}_1, \hat{\rho}_1)$ occupies the region $0 \leqslant \hat{r} \leqslant \hat{R}_1(\hat{\theta}, \hat{z}, \hat{t})$, while the second fluid (annular fluid) with viscosity and density $(\hat{\mu}_2, \hat{\rho}_2)$ occupies the region $\hat{R}_1(\hat{\theta}, \hat{z}, \hat{t}) \leqslant \hat{r} \leqslant \hat{R}_2(\hat{z})$. The equations that govern their motion, neglecting gravity, are the mass and momentum balances:

$$\nabla \cdot \underline{\hat{U}}_i = 0 \tag{3}$$

$$\hat{\rho}_i \frac{D\underline{\hat{U}}_i}{D\hat{t}} = -\nabla \hat{P}_i + \nabla \cdot \underline{\underline{\hat{\tau}}}_i \tag{4}$$

The shape of the fluid/fluid interface is determined by the kinematic condition

$$\frac{D\underline{\hat{R}}_1}{D\hat{t}} = \underline{\hat{U}}_i(\hat{R}_1(\hat{\theta}, \hat{z}, \hat{t}), \hat{\theta}, \hat{z}, \hat{t}) \tag{5}$$

where $\underline{\hat{R}}_1 = \underline{e}_r \hat{R}_1(\hat{\theta}, \hat{z}, \hat{t}) + \underline{e}_z z$ is the position vector and $\nabla(\cdot), D(\cdot)/D\hat{t}$ are the gradient operator and the substantial derivative in cylindrical coordinates, respectively. The extra stress tensor of each Newtonian fluid, $i$, is given by $\underline{\underline{\hat{\tau}}}_i = \hat{\mu}_i(\nabla \underline{\hat{U}}_i + \nabla \underline{\hat{U}}_i^T)$. In addition to being bounded at the centerline, continuous across the fluid/fluid interface and zero on the solid wall, the resulting velocity field should also satisfy the interfacial stress balance, which is expressed by the following vector equation:

$$(-\|\hat{P}\| - 2\hat{H}\hat{T})\underline{n} + \|\underline{\underline{\hat{\tau}}}\| = \underline{0} \quad \text{on } \hat{r} = \hat{R}_1(\hat{\theta}, \hat{z}, \hat{t}) \tag{6}$$

Copyright © 2002 John Wiley & Sons, Ltd. 

where $-2\hat{H} = \nabla \cdot \underline{n}|_{\hat{r}=\hat{R}_1}$ is twice the mean surface curvature of the fluid/fluid interface, $\hat{T}$ is the coefficient of surface tension, $\underline{n}$ is the unit vector normal to the surface $\hat{r} = \hat{R}_1(\hat{\theta}, \hat{z}, \hat{t})$ pointing from fluid 1 to fluid 2 and $\|\cdot\| = (\cdot)_2 - (\cdot)_1$ denotes the jump of the bracketed quantity across $\hat{r} = \hat{R}_1(\hat{\theta}, \hat{z}, \hat{t})$. In addition to the previously mentioned conditions, periodicity in both the azimuthal and axial directions is imposed on the velocity field, the stress tensor of both fluids as well as the fluid/fluid interface. We also require that the volume of the core fluid remains constant in time. The last condition that should be imposed for a well-defined set of equations is either the total volumetric flow rate of the two phases or the pressure loss. We prefer to impose the total flow rate and then compute the pressure loss along the computational domain, checking in this way the convergence of the steady solution. Whether the pressure loss or the total volumetric flow rate is imposed, the eigenvalues of the linearized equations of motion are exactly the same, which means that in either case both the total flow rate and the radially averaged pressure of a linear disturbance equal zero. However, this result does not hold in nonlinear dynamic simulations, since by keeping the *total flow rate constant*, a wavy interface develops in the nonlinear regime, which on physical grounds should increase the required pressure drop needed to keep the total flow rate constant (see Reference [11]). Imposing the flow rate of each phase leads to an ill-defined problem.

The above equations have been made dimensionless by scaling the radial direction by the maximum radius, $\hat{R}_{\max}$, of the pipe and the axial distance by $\hat{L}/2\pi$. The characteristic axial, $\hat{W}_o$, radial, $\hat{U}_o$, and azimuthal, $\hat{V}_o$, velocities are defined as follows:

$$\hat{W}_o = \hat{R}_{\max}^{-2} \left( \int_0^{\hat{R}_1} \hat{r}\hat{W}_1 \, \mathrm{d}\hat{r} + \int_{\hat{R}_1}^{\hat{R}_2} \hat{r}\hat{W}_2 \, \mathrm{d}\hat{r} \right), \quad \hat{U}_o = \hat{V}_o = \frac{\hat{R}_{\max}}{\hat{L}/2\pi} \hat{W}_o \tag{7}$$

The pressure as well as the stress components in either phase is scaled by the inertia of the core fluid, $\hat{\rho}_1 \hat{W}_o^2$ and the time by $\hat{L}/(2\pi\hat{W}_o)$. In the streamfunction-vorticity formulation, the scales for the streamfunction and the vorticity are $\hat{\Psi}_o = \hat{W}_o \hat{R}_{\max}^2$ and $\hat{\Omega}_o = \hat{W}_o/\hat{R}_{\max}$, respectively. The introduction of the above scales into Equations (1)–(6) gives rise to seven dimensionless numbers: the aspect ratio, $\Lambda = 2\pi\hat{R}_{\max}/\hat{L}$, the constriction ratio, $\alpha = \hat{R}_{\min}/\hat{R}_{\max}$, the geometric parameter $\beta$, the viscosity ratio, $\mu = \hat{\mu}_2/\hat{\mu}_1$, the density ratio, $\rho = \hat{\rho}_2/\hat{\rho}_1$, the Reynolds number, $Re = (\hat{\rho}_1 \hat{W}_o \hat{R}_{\max} \Lambda)/\hat{\mu}_1$ and the inverse Weber number, $W = \hat{T}/(\hat{\rho}_1 \hat{W}_o^2 \hat{R}_{\max})$. An additional dimensionless parameter that should be imposed is the volume fraction occupied by the core fluid, denoted as: $V = \hat{V}_1/\hat{V}_T$, where $\hat{V}_1$ and $\hat{V}_T$ are the volume occupied by the core fluid and the total volume of the tube, respectively.

## 3. ALTERNATIVE FORMULATIONS OF THE PROBLEM

### *3a. Streamfunction-vorticity formulation*

In axisymmetric flow, the streamfunction, $\hat{\Psi}_i$, and the vorticity, $\hat{\Omega}_i$, of each fluid, are defined by

$$\hat{U}_i = -\frac{1}{\hat{r}} \frac{\partial \hat{\Psi}_i}{\partial \hat{z}}, \quad \hat{W}_i = \frac{1}{\hat{r}} \frac{\partial \hat{\Psi}_i}{\partial \hat{r}}, \quad \text{and} \quad \hat{\Omega}_i = \frac{\partial \hat{W}_i}{\partial \hat{r}} - \frac{\partial \hat{U}_i}{\partial \hat{z}} \tag{8}$$

Copyright © 2002 John Wiley & Sons, Ltd. 

respectively. By cross-differentiating and subtracting the two components of the momentum balance, the pressure gradient is eliminated. The resulting dimensionless equations are:

$$r\Psi_{i,rr} - \Psi_{i,r} + \Lambda^2 r\Psi_{i,zz} - r^2\Omega_i = 0 \tag{9}$$

$$\rho_i Re\, r^2\Omega_{i,t} + (\rho_i Re\, \Psi_{i,z} + \mu_i)(\Omega_i - r\Omega_{i,r}) + \rho_i Re\, r\Psi_{i,r}\Omega_{i,z} - \mu_i r^2(\Omega_{i,rr} + \Lambda^2\Omega_{i,zz}) = 0 \tag{10}$$

$$R_1\partial_t(R_1) + R_{1,z}\Psi_{1,r}|_{r=R_1} + \Psi_{1,z}|_{r=R_1} = 0 \tag{11}$$

where $(\mu_1, \rho_1) = (1, 1)$ and $(\mu_2, \rho_2) = (\mu, \rho)$; Equation (11) is the transformed kinematic condition.

The boundary conditions along the centerline and the solid wall expressed in terms of the streamfunction and the vorticity of each fluid become:

$$\Psi_1 = -1, \quad \Psi_{1,r} = \Omega_1 = 0 \quad \text{on } r = 0 \tag{12}$$

$$\Psi_1 - \Psi_2 = \Psi_{1,r} - \Psi_{2,r} = 0 \quad \text{on } r = R_1 \tag{13}$$

$$\Psi_2 = \Psi_{2,r} = 0 \quad \text{on } r = R_2 \tag{14}$$

In addition to satisfying the boundary conditions mentioned in the previous section, Equations (12)–(14) also impose that the total dimensionless volumetric flow rate equals unity. Since the normal stress balance in Equation (6) involves the pressure, it is essential to differentiate Equation (6) with respect to the axial distance using the chain rule in order to introduce derivatives of the pressure, which are eliminated using Equation (4). In order to further simplify the boundary conditions at the axis of symmetry and the solid surface we introduce the transformations:

$$\Psi_1 = r^2\,\psi_1 - 1 \tag{15}$$

$$\Psi_2 = (r - R_2)\,\psi_2 \tag{16}$$

Consequently, we should only impose the following:

$$\psi_{1,r} = 0 \quad \text{on } r = 0 \tag{17}$$

$$R_1^2\,\psi_1 - (R_1 - R_2)\,\psi_2 = 1, \quad 2R_1\,\psi_1 - \psi_2 + R_1^2\,\psi_{1,r} - (R_1 - R_2)\,\psi_{2,r} = 0 \quad \text{on } r = R_1 \tag{18}$$

$$\psi_2 = 0 \quad \text{on } r = R_2 \tag{19}$$

The advantage of these transformations is that we only have to use four boundary conditions, Equations (17)–(19), instead of seven, Equations (12)–(14), since three of them are satisfied implicitly. As a result, Equations (17) and (19) are imposed as boundary conditions at the centerline and the solid wall, respectively, while Equations (18) are imposed as boundary conditions on the fluid/fluid interface, all related to the streamfunction. In their final form, the interfacial force balances involve first derivatives of vorticity and they are imposed as boundary

Copyright © 2002 John Wiley & Sons, Ltd. 

conditions to the vorticity equation on the fluid/fluid interface, while at the centerline and the solid wall (Equation (9)), is imposed as a boundary condition to the vorticity equation [12].

The application of the constant volume of core fluid is related to the periodic boundary conditions. In order to make this clear we integrate Equation (11) over the computational length to obtain:

$$\frac{\mathrm{d}}{\mathrm{d}t}\left(\int_0^{2\pi} R_1^2\,\mathrm{d}z\right) + 2\int_0^{2\pi} \mathrm{d}(\Psi_1|_{r=R_1}) = 0 \tag{20}$$

Upon applying the periodic boundary condition, we obtain $\int_0^{2\pi} R_1^2\,\mathrm{d}z = \text{constant}$. Thus, the volume of the core fluid remains constant in time and, because it is an integral form of the kinematic equation along the considered tube length, the kinematic condition is dropped at one of the grid points in the interface and Equation (20) is imposed instead.

### *3b. Primitive formulation*

When the system of Equations (3)–(5) is solved subject to the appropriate boundary conditions in the primitive formulation, we perform the following transformation, irrespective of the adopted numerical method of solution:

$$P_i = p_i + \Delta P z \tag{21}$$

This transformation [4, 13] is used in order to decompose the original pressure term $P_i$ into a periodic part $p_i$ and a term $(\Delta P z)$ that varies linearly with the axial distance. In this way, we make explicit the pressure drop per unit length, $\Delta P$, which is calculated by satisfying that the total volumetric flow rate, which in dimensionless form reduces to $\int_0^{R_1} rW_1\,\mathrm{d}r + \int_{R_1}^{R_2} rW_2\,\mathrm{d}r = 1$, remains constant [14]. The imposition of the constant volume of the core fluid is implemented in the same way as explained in the streamfunction-vorticity formulation (Equation (20)).

It is worth mentioning that, in the case of stability with respect to non-axisymmetric disturbances, different boundary conditions should be imposed on the perturbation functions (denoted by the subscript $p$) at the axis of symmetry, depending on the wavenumber in the azimuthal direction, $k$. There are different ways to obtain the appropriate boundary conditions at the centerline. One may use the Frobenious method or may start from requiring that the velocity field is single-valued at the centerline [15]. Finally, one may take the limit of the momentum and continuity equations as the radial distance goes to zero, and then recover the conditions that guarantee the boundedness of the velocity field by using L'Hospital's rule. Following any of these routes, the resulting conditions at the centerline are:

$$\begin{aligned}
&\text{Radial velocity:} && k \neq 1,\ U_{1,p} = 0;\ k = 1,\ U_{1,p} + iV_{1,p} = 0\\
&\text{Azimuthal velocity:} && k = 1,\ \partial_r V_{1,p} = 0;\ k \neq 1,\ V_{1,p} = 0\\
&\text{Axial velocity:} && k = 0,\ \partial_r W_{1,p} = 0;\ k \neq 0,\ W_{1,p} = 0
\end{aligned} \tag{22}$$

## 4. NUMERICAL IMPLEMENTATION

The steady axisymmetric eigenvalue problem is solved using three methods: (i) a pseudo-spectral method in the streamfunction-vorticity formulation, denoted by SVFSM; (ii) adopting

Copyright © 2002 John Wiley & Sons, Ltd. 

again a pseudo-spectral method in the primitive formulation, PFSM; and (iii) using the finite element method in primitive formulation, PFFEM. In order to properly discretize the physical domain and correctly impose the interfacial boundary conditions onto the fluid/fluid interface and the solid wall, the following coordinate normalization is implemented, irrespective of the numerical method of solution:

$$\text{Fluid 1:} \quad x_1 = 1 - 2\frac{r}{R_1(\theta,z,t)}, \quad x_2 = \theta, \quad x_3 = z, \ \tau = t \tag{23}$$

$$\text{Fluid 2:} \quad x_1 = -1 + 2\frac{r - R_1(\theta,z,t)}{1 - R_1(\theta,z,t)}, \quad x_2 = \theta, \quad x_3 = z, \ \tau = t \tag{24}$$

This non-orthogonal, body-fitted coordinate transformation $(r,\theta,z,t) \rightarrow (x_1,x_2,x_3,\tau)$ has been employed in order to map the *a priori* unknown, time-dependent regions occupied by each fluid onto the fixed $x_1 = -1$ plane, while the centerline and the solid wall are mapped onto the $x_1 = 1$ plane. Thus, the bounds of the new independent variables are $-1 \leqslant x_1 \leqslant 1$, $0 \leqslant x_2$, $x_3 \leqslant 2\pi$, and $\tau \geqslant 0$. Of course, this transformation is valid only when the function $R_1 = R_1(\theta,z,t)$ is single valued and it breaks down when folding of the interface occurs.

### *4a. Pseudo-spectral method*

When the pseudo-spectral method is used (SVFSM and PFSM), every dependent variable is approximated using Chebyshev polynomials in the $x_1$ direction and Fourier modes in the $x_3$ direction so that the periodic boundary conditions in the axial direction are satisfied implicitly. The grid points in the $x_1$ direction are defined as the extreme of the highest-order Chebyshev polynomial that we use ($M$), while the grid points in this direction are given by: $x_{1,m} = \cos(\pi(m-1)/(M-1))$, $1 \leqslant m \leqslant M$. The grid points in the $x_3$-direction are taken to be equidistant, i.e. $x_{3,n} = 2\pi(n-1)/N$, $1 \leqslant n \leqslant N$. So, every dependent variable is approximated as a sum of products of Chebyshev polynomials, $C_i(x_1)$, and Fourier modes, $F_j(x_3)$,

$$f(x_1,x_3) = \sum_{i=1}^{M}\sum_{j=1}^{N} a_{ij} C_i(x_1) F_j(x_3) \tag{25}$$

The unknowns, $a_{ij}$, are computed by direct satisfaction of the differential equations at the collocation points. Whereas the use of the streamfunction-vorticity formulation alleviates the problem of dealing with the incompressibility constraint, the solution of the Navier–Stokes equations in the primitive variables requires special treatment of the pressure variable. Canuto *et al.* [16] suggest that the pressure variable needs a special treatment, when the flow domain involves inhomogeneous directions, which is the case with the radial direction here. More specifically, they report that the spectral expansion of the pressure should be at least one order lower than the expansion used for the velocity field, and the pressure should be computed at collocation points staggered with respect to those at which the radial and axial momentum balances are enforced. This is necessary because the pressure term arises in the evolution equations of the velocities in the form of first derivatives only and not in the continuity equation. Therefore, the use of the same approximation for both the pressure and the velocity will lead to an underdetermined set of equations. In particular, there are two parasitic modes that enter the discrete set, when all variables are approximated by polynomials of the same order: the constant term in the representation for pressure, and the highest

Copyright © 2002 John Wiley & Sons, Ltd. 

order polynomial which has zero first derivative in all the internal collocation points, but not at the boundaries. Thus, these two modes cannot affect either the momentum equations or the continuity equation and, as a result, they remain undetermined. Of course, the use of a staggered mesh can circumvent this problem at the expense of increased programming complexity, since apart from projecting each variable at the collocation points of the other variables, the boundaries need special treatment in order to impose the relevant boundary conditions.

We choose to approximate the pressure and the velocity components with Chebyshev polynomial expansions of the same order. The two parasitic modes for the pressure in each phase cannot be calculated using the continuity equation as explained above and, thus, we are obliged to drop this equation at the centerline, at the interface between the two fluids as well as at the solid surface. Instead of them, we enforce the radial momentum equation, which would not be used otherwise, because it is substituted by the no-penetration condition at the solid wall and the appropriate conditions at the centerline and the interface. In addition, at one collocation point at the solid wall and the entrance of the tube we impose the pressure datum, $p_2 = 0$. Thus, the inconsistencies are removed, and the set of equations is no longer underdetermined. Canuto *et al*. [16] suggest that when a non-staggered mesh is used then conditions consistent with the incompressibility constraint should be enforced at the boundaries as well. This is similar to what we have done.

We have checked *a posteriori* the numerical error with which the omitted continuity equations are satisfied and we have found it to be always slightly higher ($\sim 10^{-8}$) than the predefined error, set for the rest of the equations, and to decrease with mesh refinement. Moreover, we have checked independently both the steady solutions and the axisymmetric eigenvalues computed using this formulation with those using the SVFSM and PFFEM and have found complete agreement in all cases. We have performed further testing by computing non-axisymmetric eigenvalues assuming straight tube geometry and the results have always been in complete agreement with the ones that we report in the following sections.

### *4b. Finite element method*

When the Galerkin finite element method is used, PFFEM, the computational domain is partitioned uniformly into quadrilateral elements. A mixed formulation is applied for the approximation of the velocity and the pressure fields [17]. In particular, the independent variables and the velocity field of each fluid are represented by biquadratic, the pressure by bilinear and the fluid/fluid interface by quadratic Lagrangian basis functions, i.e.:

$$\begin{aligned} p_i(x_1,x_3) &= \sum_j p_i^j L^j(\xi,\eta), \quad \underline{U}_i(x_1,x_3) = \sum_j \underline{U}_i^j Q^j(\xi,\eta) \\ R_1(x_3) &= \sum_j R_1^j q^j(\xi), \quad -1 \leqslant \xi,\eta \leqslant 1 \end{aligned} \tag{26}$$

The momentum and continuity equations for each fluid are weighed with the biquadratic, $Q^j(\xi,\eta)$, and bilinear, $L^j(\xi,\eta)$, basis functions, respectively, and then integrated over the volume that each fluid occupies. The kinematic equation is weighed with the quadratic basis functions, $q^j(\xi)$, and then integrated along the axial distance. The resulting two dimensional integrals are evaluated using nine Gauss points and the one-dimensional ones using the three-point Gaussian quadrature. The momentum equation involves the divergence of the stress

Copyright © 2002 John Wiley & Sons, Ltd. 

tensor and requires application of the divergence theorem within each element in order to reduce the order of the velocity derivatives from two to one. The resulting line integrals on fluid boundaries are either omitted in order to impose essential conditions (no slip, no penetration at the solid wall, condition at the centerline and periodicity) or computed by the interfacial stress balance. The mean curvature has to be specially treated as it involves products of the interface position with its second derivative. Using the methodology proposed by Ruschak [18] and applied by Poslinski and Tsamopoulos [19], the mean curvature on the interface is split into two parts. The first term is the derivative of the tangent vector ($t$) of the interface with respect to its arc length ($s$), while the second part is composed of the normal vector multiplied by the inverse of the second principal radius $R = R_1\sqrt{1 + \Lambda^2 R_{1,zz}^2}$.

$$-2H\underline{n} = -\frac{\mathrm{d}\underline{t}}{\mathrm{d}s} + \frac{\underline{n}}{R} \tag{27}$$

In this form the curvature operator is introduced in the momentum equations through the following:

$$\oint_S \underline{n}\cdot(\underline{\underline{\tau}}_1 - \underline{\underline{\tau}}_2)Q^j\,\mathrm{d}s = W\Lambda\int (R_{1,z}q^j + R_1 q_z^j)\frac{\underline{e}_z + \Lambda R_{1,z}\underline{e}_r}{\sqrt{1+\Lambda^2 R_{1,z}^2}}\,\mathrm{d}z + W\int \frac{\underline{e}_r - \Lambda R_{1,z}\underline{e}_z}{\sqrt{1+\Lambda^2 R_{1,z}^2}}q^j\,\mathrm{d}z + \int (\underline{e}_r - \Lambda R_{1,z}\underline{e}_z)(p_1 - p_2)q^j\,\mathrm{d}z \tag{27a}$$

The left-hand-side of Equation (27a) is the surface integral of the stress difference between the two fluids, which results from the application of the Gauss theorem on the momentum equations. As dictated by the interfacial force balance this term is replaced by the right-hand-side the first two terms of which account for capillarity, while the third one accounts for the pressure jump across the interface.

## 5. NUMERICAL SOLUTION

The Newton–Raphson technique is utilized in order to solve the resulting non-linear system of algebraic equations irrespective of the method used to convert the differential equations into algebraic ones. In the case of the finite element method, the entries of the Jacobian matrix are calculated using analytical expressions. The Jacobian matrix has an arrow-shaped structure, which is taken into account in order to minimize the storage requirements and to accelerate the computations during Gauss elimination [19]. Our solver is a combination of the one used by Poslinski and Tsamopoulos [19] with the commercially available BLAS routines, which leads to a 25 per cent reduction of the execution time. The convergence criterion is that the Euclidean norm of the residuals is less than $10^{-11}$. In the case of the spectral method, the entries of the matrix are computed numerically using one-sided finite differences, the step of which is given by $0.5\times 10^{-8}\max(1, abs(a_i))$, where $(a_i)$ is the $i$th unknown. The steady solutions are computed using a dense matrix solver because the resulting Jacobian matrix is now fully populated. The convergence criterion in this case is that the maximum residual is less than $10^{-10}$.

Copyright © 2002 John Wiley & Sons, Ltd. 

Upon computing the steady solution, denoted by the subscript $s$, its stability is examined. To this end, we perturb the steady solution allowing for 2D or 3D disturbances,

$$\begin{bmatrix} \Psi_i(x_1,x_3,\tau) \\ \Omega_i(x_1,x_3,\tau) \\ R_1(x_3,\tau) \end{bmatrix} = \begin{bmatrix} \Psi_{i,s}(x_1,x_3) \\ \Omega_{i,s}(x_1,x_3) \\ R_{1,s}(x_3) \end{bmatrix} + \delta \begin{bmatrix} \Psi_{i,p}(x_1,x_3) \\ \Omega_{i,p}(x_1,x_3) \\ R_{1,p}(x_3) \end{bmatrix} \exp(\sigma\tau) \tag{28}$$

$$\begin{bmatrix} U_i(x_1,x_2,x_3,\tau) \\ W_i(x_1,x_2,x_3,\tau) \\ p_i(x_1,x_2,x_3,\tau) \\ R_1(x_2,x_3,\tau) \end{bmatrix} = \begin{bmatrix} U_{i,s}(x_1,x_3) \\ W_{i,s}(x_1,x_3) \\ p_{i,s}(x_1,x_3) \\ R_{1,s}(x_3) \end{bmatrix} + \delta \begin{bmatrix} U_{i,p}(x_1,x_3) \\ W_{i,p}(x_1,x_3) \\ p_{i,p}(x_1,x_3) \\ R_{1,p}(x_3) \end{bmatrix} \exp(\sigma\tau + ikx_2) \tag{29}$$

respectively, where the subscript $p$ denotes the disturbances. By omitting terms of order higher than the perturbation parameter $\delta$, we obtain a generalized eigenvalue problem of the form $\underline{\underline{J}}\ \underline{x} = \sigma \underline{\underline{M}}\ \underline{x}$, where $\underline{\underline{J}}$ and $\underline{\underline{M}}$ are the Jacobian and the mass matrix, respectively. The eigenvalues, $\sigma$, are generally complex. The real part of $\sigma$, $Re(\sigma)$, corresponds to the growth rate of the disturbance, while its imaginary part, $Im(\sigma)$, corresponds to the temporal oscillation frequency. The steady state is stable to infinitesimal disturbances, if the real parts of all the eigenvalues are negative; otherwise it is said to be unstable. In order to reduce the requirements for storing two square matrixes, the above generalized eigenvalue problem has been transformed to the standard one:

$$(\underline{\underline{J}}^{-1}\underline{\underline{M}})\underline{x} = \frac{\sigma^*}{\|\sigma\|^2}\underline{x} \tag{30}$$

where $(^*)$ denotes the complex conjugate. The Jacobian matrix is invertible unless there is at least one zero eigenvalue. On the other hand, the mass matrix is always non-invertible, since the vorticity and the continuity equation, in addition to some boundary conditions, involve no time derivatives. The resulting eigenvalue problem is solved using Arnoldi's method [20] (see, for example, Sureshkumar and Beris [21] and Kouris and Tsamopoulos [7] for the implementation of Arnoldi's algorithm). The algorithm we have used is based on the commercially available software developed by Lehoucq and Scott [20], which is capable by default of computing the eigenvalues with large magnitudes. However, this is not what is needed here, since the eigenvalues of interest are those with the smallest real parts. On the other hand, we have observed that when the most 'dangerous' modes are those with long wavelength (when $Re \ll 1$), the software is capable of locating those with the smaller real parts if only 10–20 modes with the largest magnitudes are computed. Furthermore, when $Re \gg 1$, the unstable modes are characterized by short wavelength with large temporal frequencies. In this case, the number of the computed eigenvalues should be increased up to 300.

With $M$ Chebyshev modes in the radial direction and $N$ Fourier modes in the axial direction for each phase, the total number of unknowns is $4MN+N$ $(\Omega_{i,s}, \Psi_{i,s}, R_{i,s})$ with the SVFSM, and $6MN+N$ $(U_{i,s}, W_{i,s}, P_{i,s}, R_{1,s})$ with the axisymmetric PFSM. In the case of the non-axisymmetric PFSM ($k \neq 0$), i.e., when the eigenvalues of the complex variables $(U_{i,p}, W_{i,p}, V_{i,p}, P_{i,p}, R_{1,p})$ are calculated, the total number of unknowns is $2(8MN + N)$. This last formulation leads to a considerable increase in unknowns, but it is necessary in order to examine the stability of the

Copyright © 2002 John Wiley & Sons, Ltd. 

base flow to three-dimensional disturbances. Finally, with the PFFEM, $M$ radial elements and $N$ axial ones are used in each phase, and the total number of unknowns is $4(2M+1)(2N+1)+2(M+2)(N+1)$.

Regardless of the numerical scheme of solution or the adopted formulation, the time integration is performed using the implicit Euler method with constant time step equal to $0.5\times10^{-3}$. In order to accelerate the time integration, the modified Newton–Raphson technique is introduced, i.e. the solution at the current time step is found using the $LU$ decomposed Jacobian matrix corresponding to a previous time step up to a point that the convergence rate becomes less than linear. It is worth saying that for the examined set of dimensionless numbers, the time integration using both SVFSM and PFFEM does not produce fictitious oscillations. In particular, the SVFSM numerical scheme of solution has been used extensively in examining the linear stability of CAF in constricted tubes [6, 7] and its nonlinear dynamics in straight tubes [22, 23]. In some of these cases, the dynamic response of the system has been polluted by fictitious oscillations, which have been removed using a filtering technique. With the present parameter values, we have not encountered such problems, but still we have integrated the time dependent partial differential equations using our filtering technique, which is slightly different than that proposed by Avgousti *et al.* [24]. This is done in order to assess the effect of the filter on the time evolution of the two-phase flow by comparing the initial dynamic response with the growth rate and the temporal frequency computed using the linear stability theory. Avgousti *et al.* [24] suggest that each dependent variable follows certain regular patterns with respect to the mode number, provided that the spatial variation of these variables is smooth enough. The spectrum of these modes is divided into three frequency parts. The amplitude of the lower part follows closely the transient variation, the amplitude of the intermediate part decreases with increasing the mode number, and the upper part varies unpredictably due to numerical error. Although the upper part of the spectrum is insignificant, it is the primary cause for inducing numerical instabilities, as these artifacts are always associated with large amplitudes of the high frequency modes. In their work, Avgousti *et al.* [24] propose either an exponential cutoff filter or a procedure called spectrum regularization. Instead, we choose to completely damp the upper third of the spectrum at every time step. To achieve this, we decompose the solution into its Fourier modes, set the highest third of them to zero, and then reconstruct the solution at every collocation point using the remaining two thirds of the Fourier modes. In this way, the high frequency modes are completely damped (see also Beris and Sureshkumar [25]).

## 6. RESULTS AND DISCUSSION

In our numerical experiments we impose a constant total volumetric flow rate. We first compute the basic flow field and then the pressure loss along the tube. Subsequently, the stability of the steady solution is examined by solving for the most dangerous eigenvalues of the linearized equations. We are interested in the assessment of the two formulations (streamfunction-vorticity versus primitive variables) and of the two numerical methods (pseudo-spectral versus finite elements). To this end, we have focused our attention on the effect of the Reynolds number on the total number of unknowns, which each formulation requires for the accurate representation of both the steady solution and the most unstable disturbance in the axisymmetric case. A complete parametric study has been presented elsewhere [6, 7]. In order to

Copyright © 2002 John Wiley & Sons, Ltd. 

quantify the term 'accurate representation', we define an objective function to measure the absolute difference of the approximate solution from that corresponding to the finest mesh used, the 'exact result'. Although this choice is arbitrary and may introduce round-off errors into the calculations, which may affect the convergence rates of the numerical methods, it is the best available.

The pressure drop, which is the most sensitive variable, is used to compute the relative error in the steady-state calculations. This error, $RE^{SC}$, is defined as the absolute value of the difference between the pressure drop in various resolutions minus its 'exact' value divided by the absolute value of its 'exact' value:

$$RE^{SC} = \left| 1 - \frac{\Delta P}{\Delta P_{\mathrm{EXACT}}} \right| \tag{31}$$

In the eigenvalue calculations, the relative error ($RE^{EC}$) is defined as the absolute value of the difference between the real part of the most unstable eigenvalue minus the real part of the 'exact' eigenvalue, normalized by the modulus of the 'exact' eigenvalue, i.e.:

$$RE^{EC} = \frac{|Re(\sigma_{\mathrm{EXACT}}) - Re(\sigma)|}{\sqrt{Re(\sigma_{\mathrm{EXACT}})^2 + Im(\sigma_{\mathrm{EXACT}})^2}} \tag{32}$$

The results presented in the figures correspond to the following values of the dimensionless numbers: $\alpha = 0.55$, $\Lambda = \pi/2$, $V = 0.7988$, $\mu = 0.05$ and $\rho = 1$. We use a small value for $\mu$ in order to promote separation of the steady flow of the outer fluid at relatively small values of the Reynolds number [7]. We also use a small value for the inverse Weber number in order to induce unstable modes of short-wavelength whose accurate representation is a difficult numerical task. The other parameter that we vary in our numerical experiments, besides the tube geometry, is the Reynolds number. In all the figures that present streamlines of the basic flow, the streamfunction at the axis of symmetry, $r = 0$, equals $-1$, the streamfunction at the solid wall, $r = R_2$, equals 0, while the thick line indicates the position of the fluid/fluid interface.

### *6a. Comparison of methods in steady and eigenvalue calculations*

The lower half of Figure 1 shows the streamlines of the basic, steady flow for $Re = 1$. Flow takes place from left to right. It is clear that the streamlines smoothly follow the solid wall and they appear to be symmetric around the mid-plane of the tube. The value of the streamfunction at the interface is $\Psi_1 = -0.0935$. The upper part of Figure 1 shows contour lines of the periodic part of the pressure field for the steady flow, as computed using the PFSM scheme. The maximum (minimum) of the periodic part of the pressure occurs in the annular fluid, near the tube wall and at the center of the right (left) closed curve and has a value of $p_2 = 48.9$ $(-16.9)$. There is a jump in the pressure across the interface, which is induced by the capillary force. An interesting observation is that, although the streamlines appear to be symmetric around the mid-plane of the tube, this does not hold for the periodic part of the pressure. This result means that even the velocity field is not symmetric and, in this case, the asymmetry is more clearly identifiable in the pressure field, which is a more sensitive indicator than the streamlines. The asymmetry is caused by the small but not negligible Reynolds number. The effect of the latter is amplified by the fairly small constriction ratio which forces the fluids to decelerate as they enter the expanding portion of the tube,

Copyright © 2002 John Wiley & Sons, Ltd. 

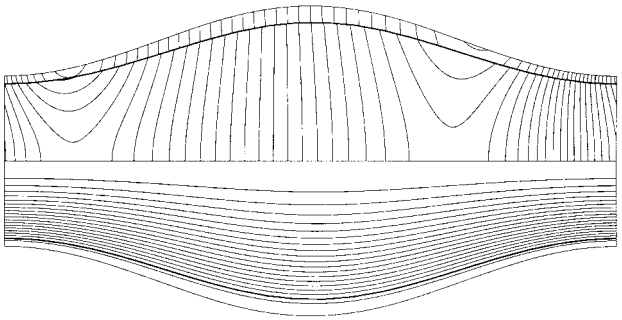

Figure 1. Contour lines of both the pressure (upper half) and the streamfunction (lower half) of the steady solution for $(\alpha, \Lambda, \beta, V, \mu, \rho, Re, W) = (0.55, \pi/2, 0, 0.7988, 0.05, 1, 1, 0.05)$.

and then to accelerate as they exit it through its contracting portion. In the same figure, we can also identify two distinct regions in the pressure field where contour lines end at the tube wall. As *Re* tends to zero, the region located closer to the entrance of the tube moves backwards so that one half of it occupies the entrance and the other half the exit of the tube. Similarly, the region, which can be seen to the right of the mid-plane of the tube, also moves backwards and in such a way that all field variables regain symmetry around the mid-plane. The converged value of the pressure loss per unit length is $\Delta P = -13.69063$, and the most dangerous eigenvalue is found to be $\sigma = 0.28084 \times 10^{-1} \pm 0.665008 \times 10^{1}$i, i.e., the steady flow is unstable.

Figures 2–4 present the convergence rates using different formulations and numerical methods. Figures 2(a), (2(b)) and 3(a), (3(b)) show the convergence rate with respect to the highest order of the retained Chebyshev polynomial (Fourier mode), when the equations of motion are expressed in terms of the streamfunction-vorticity and in primitive variables, respectively. The common characteristic of these figures is that there is an exponential decrease in the relative error of both the steady and the eigenvalue problems. Although the convergence rates for these two problems are large and approximately similar up to a certain number of modes, the relative errors attain plateaus as the number of modes is increased. In the steady case, the plateau arises at a relative error of $\sim 10^{-11}$, which is easily explained by taking into account the round-off error and the tolerance used for the Newton–Raphson process. In the eigenvalue calculations, the relatively large value of the error in the computations of the most unstable eigenvalue is probably caused by the error introduced by the numerical computation of the Jacobian matrix. Figures 2(b) and 3(a), demonstrate that the line corresponding to the eigenvalue problem is shifted upwards by about two orders of magnitude with respect to its steady-state counterpart. In Figure 3(b), the two lines virtually coincide, indicating that the same relative error occurs in both the steady and the eigenvalue problem. Comparing Figures 2(a), (b) and 3(a), (b) we see that 15 Fourier modes and nine Chebyshev modes are needed in order to decrease the error below $10^{-5}$ for both the steady and the eigenvalue problem. This fact makes the SVFSM much more efficient than the PFSM as the former involves fewer unknowns.

The variation of the relative error in the PFFEM formulation with the number of elements in the radial and axial directions can be seen in Figures 4(a) and (b). Apparently, the convergence rates are lower than those obtained with the spectral methods, following a relation of the form:

Copyright © 2002 John Wiley & Sons, Ltd. 

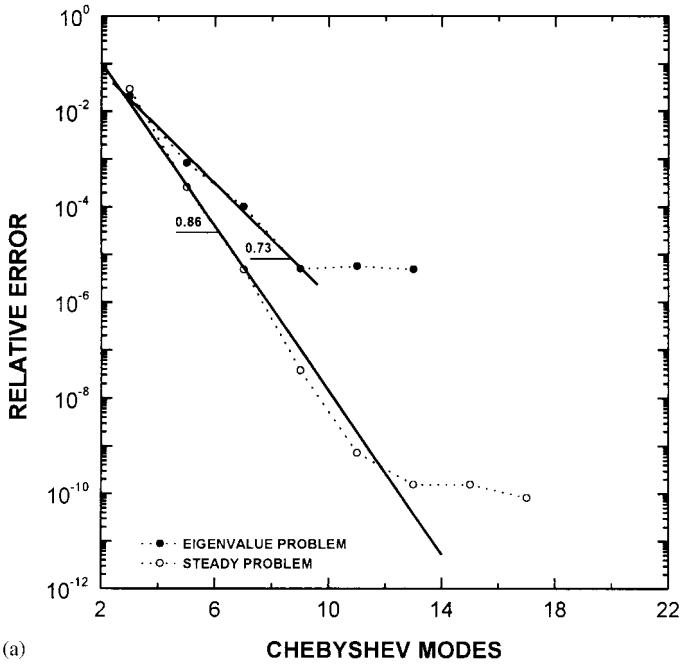


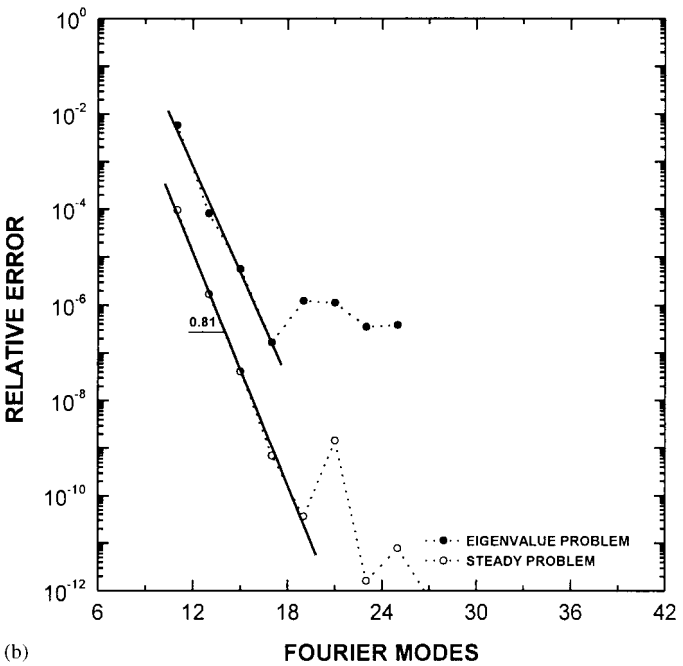


Figure 2. Variation of the relative error with respect to the (a) Chebyshev modes for 19 Fourier modes and (b) Fourier modes for 13 Chebyshev modes using the SVFSM for $(\alpha, \Lambda, \beta, V, \mu, \rho, Re, W) = (0.55, \pi/2, 0, 0.7988, 0.05, 1, 1, 0.05)$.

Copyright © 2002 John Wiley & Sons, Ltd. 

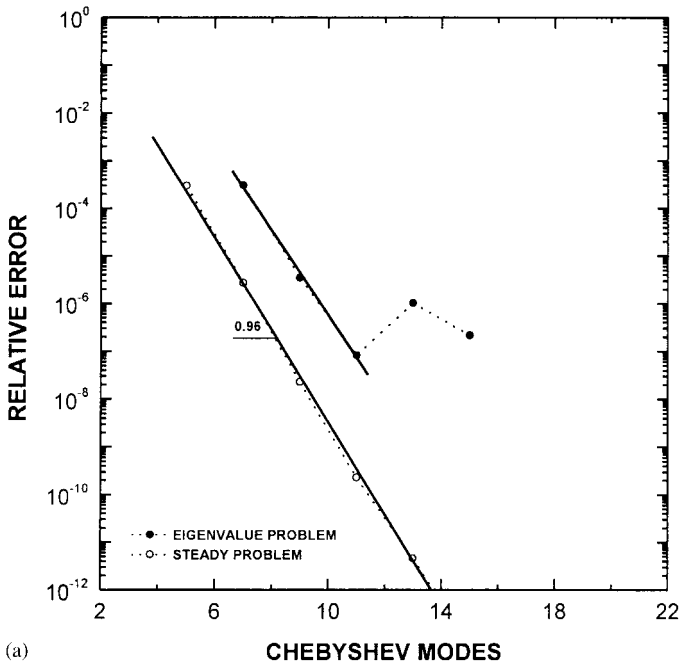


(a)

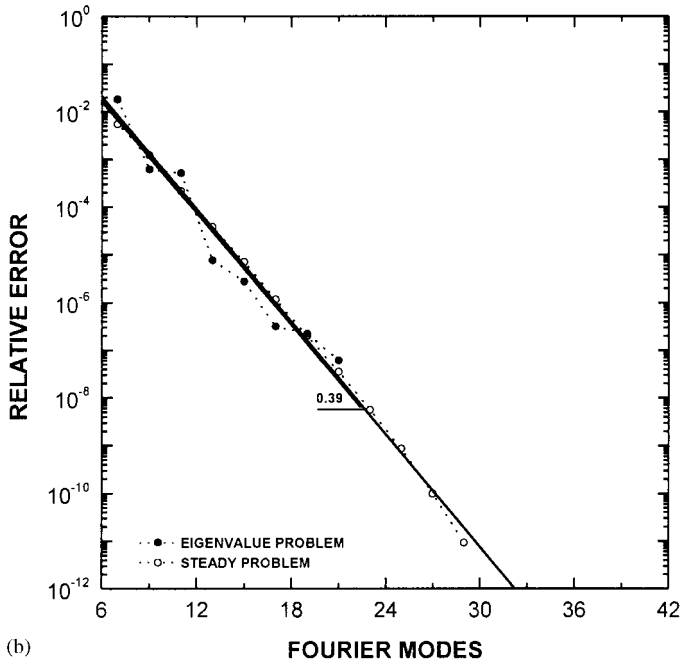


(b)

Figure 3. Variation of the relative error with respect to the (a) Chebyshev modes for 21 Fourier modes and (b) Fourier modes for nine Chebyshev modes using PFSM for $(\alpha, \Lambda, \beta, V, \mu, \rho, Re, W) = (0.55, \pi/2, 0, 0.7988, 0.05, 1, 1, 0.05)$.

Copyright © 2002 John Wiley & Sons, Ltd. 

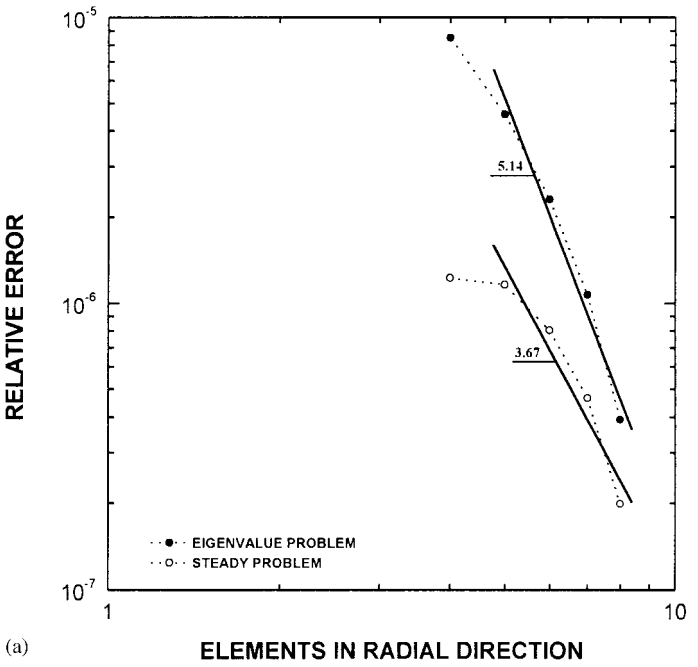


(a)

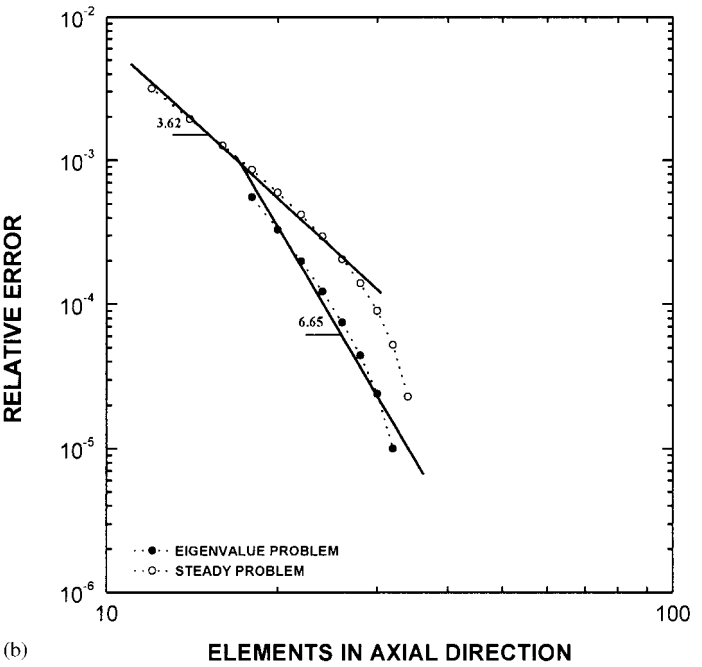


(b)

Figure 4. Variation of the relative error with respect to the number of (a) radial elements using 26 axial and (b) axial elements using six radial elements; PFFEM, for $(\alpha, \Lambda, \beta, V, \mu, \rho, Re, W) = (0.55, \pi/2, 0, 0.7988, 0.05, 1, 1, 0.05)$.

Copyright © 2002 John Wiley & Sons, Ltd. 

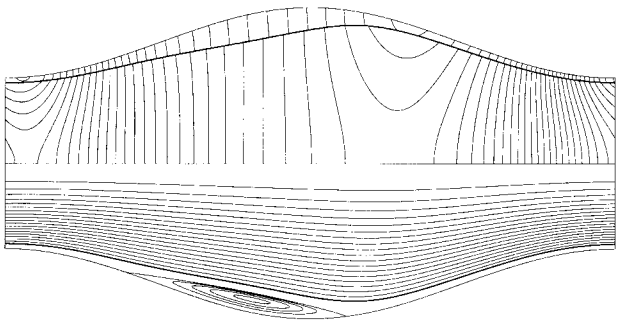

Figure 5. Contour lines of both the pressure (upper half) and the streamfunction (lower half) of the steady solution for $(\alpha, \Lambda, \beta, V, \mu, \rho, Re, W) = (0.55, \pi/2, 0, 0.7988, 0.05, 1, 7.5, 0.05)$.

Error $\sim c_1 h^k \sim c_2 N^{-k}$, where $c_1$ and $c_2$ are constants, $h$ is a measure of the element size, $N$ is the number of elements and $k$ is the convergence rate. Clearly, the convergence rate becomes algebraic instead of exponential, a fact that is known from previous theoretical investigations. Nevertheless, the convergence rates we obtained are above the theoretical predictions (e.g., Osborn [26]): 3.67 instead of the theoretical value of 2 for the steady state problem, and 5.14 instead of 4 for the linearized eigenvalue problem. In order to assess the efficiency of each numerical method, we set a relative error of $10^{-4}$ and then by using Figures 2–4 we reach the conclusion that 377, 715 and 2568 unknowns are needed using the SVFSM, PFSM and PFFEM, respectively. Obviously, in the case of small Reynolds number, the use of a spectral representation and the primitive variable formulation results in a 70 per cent reduction of the total number of unknowns compared with the PFFEM. Additional reductions can be achieved by exploiting the axial symmetry of the problem and using the SVFSM scheme as the reduction in the number of the unknowns is greater than 85 per cent over the PFFEM. However, the storage requirements for the PFFEM formulation in the steady state case are lower, due to the arrow-shaped structure of the Jacobian matrix (see Section 4). We have not taken advantage of this matrix structure for the eigenvalue calculations, although this is possible by increasing considerably the code complexity, instead matrices are stored and used assuming that their shape is square. In eigenvalue calculations, the computational cost depends on the square of the number of unknowns and, thus, the computation of the same number of eigenvalues using the PFSM and PFFEM formulations require 3.6 and 46 times more computational time than the SVFSM.

Next, we increase the Reynolds number to $Re = 7.5$ and present in Figure 5 both the streamlines and the periodic part of the pressure (computed using PFSM) which correspond to the steady flow. The value of the streamfunction at the center of the vortex is 0.0129, while that at the interface is $-0.0539$. The converged value of the pressure loss per unit length is $\Delta P = -2.435416$ and the maximum (minimum) value of the periodic part of the pressure is $p_2 = 27.6$ $(-0.8)$. The most dangerous eigenvalue is found to be $\sigma = 0.5104 \pm 0.52978 \times 10^1$i, i.e., the linear growth rate has increased. It can also be seen that, at this higher $Re$ value, flow separation occurs and recirculation develops in the outer fluid in the expanding portion of the tube, while the asymmetry of the pressure field is further intensified. Figures 6–8 show the convergence of the most unstable eigenvalue and the pressure loss with the number of the used modes or elements. An observation that should be made concerning Figures 6

Copyright © 2002 John Wiley & Sons, Ltd. 

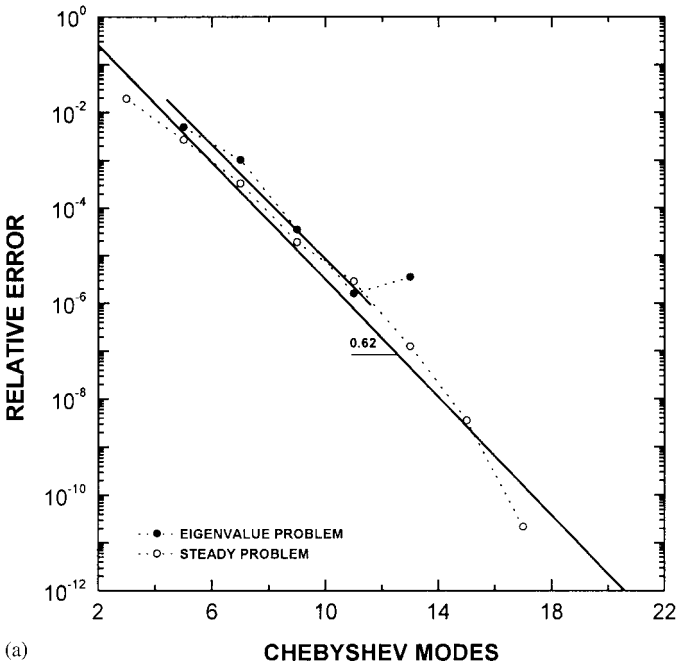


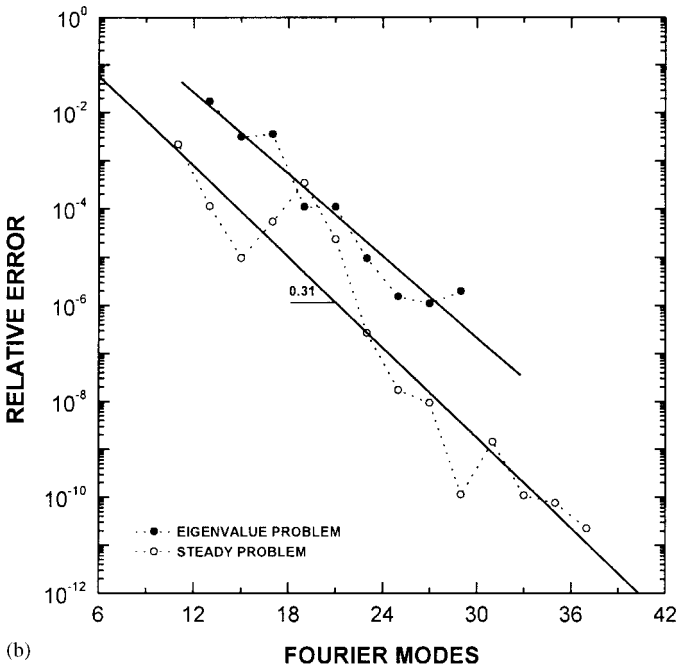


Figure 6. Variation of the relative error with respect to the (a) Chebyshev modes for 25 Fourier modes and (b) Fourier modes for 15 Chebyshev modes; SVFSM, for $(\alpha, \Lambda, \beta, V, \mu, \rho, Re, W) = (0.55, \pi/2, 0, 0.7988, 0.05, 1, 7.5, 0.05)$.

Copyright © 2002 John Wiley & Sons, Ltd. 

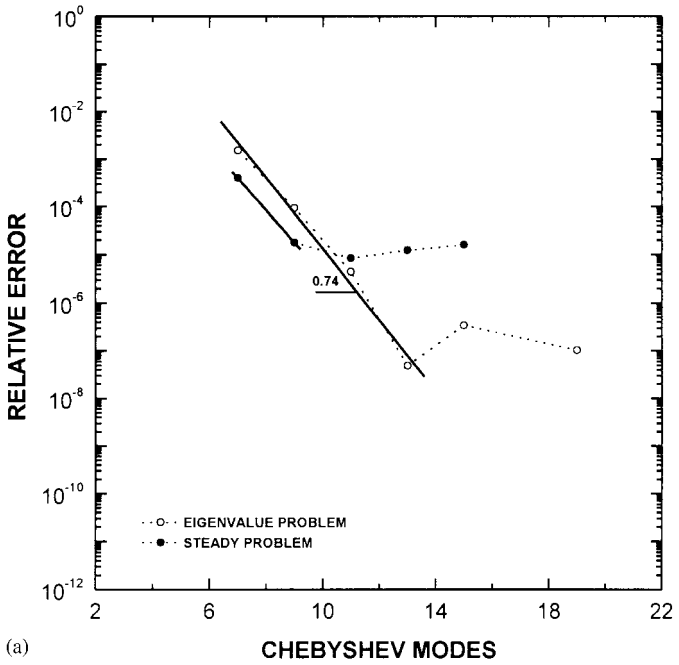


(a)

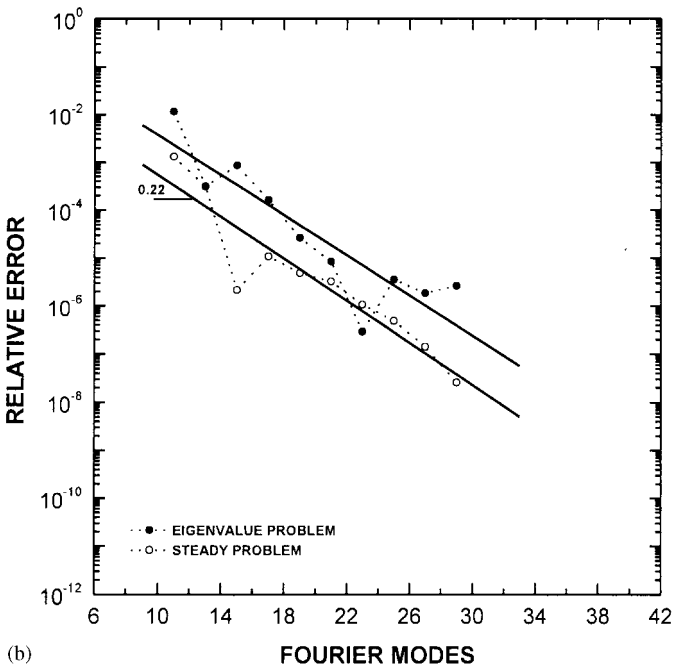


(b)

Figure 7. Variation of the relative error with respect to the (a) Chebyshev modes for 21 Fourier modes and (b) Fourier modes for 13 Chebyshev modes; PFSM, for $(\alpha, \Lambda, \beta, V, \mu, \rho, Re, W) = (0.55, \pi/2, 0, 0.7988, 0.05, 1, 7.5, 0.05)$.

Copyright © 2002 John Wiley & Sons, Ltd. 

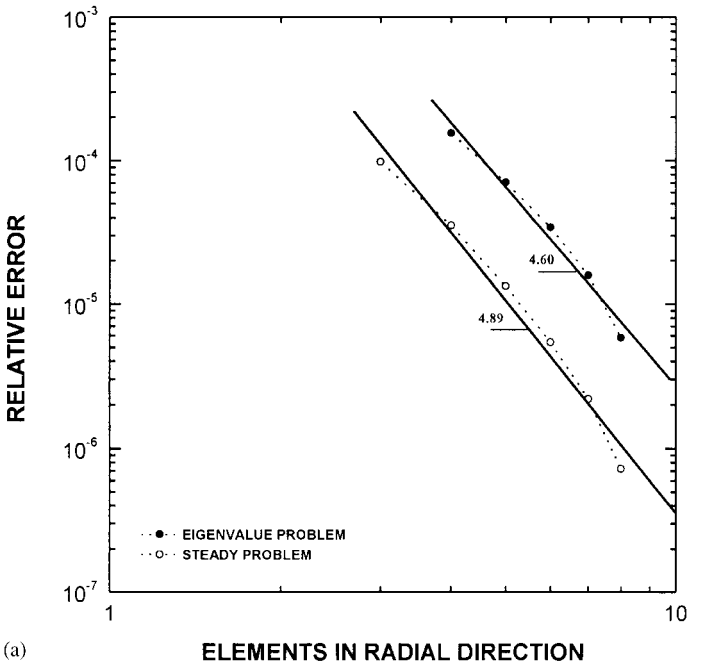


(a)

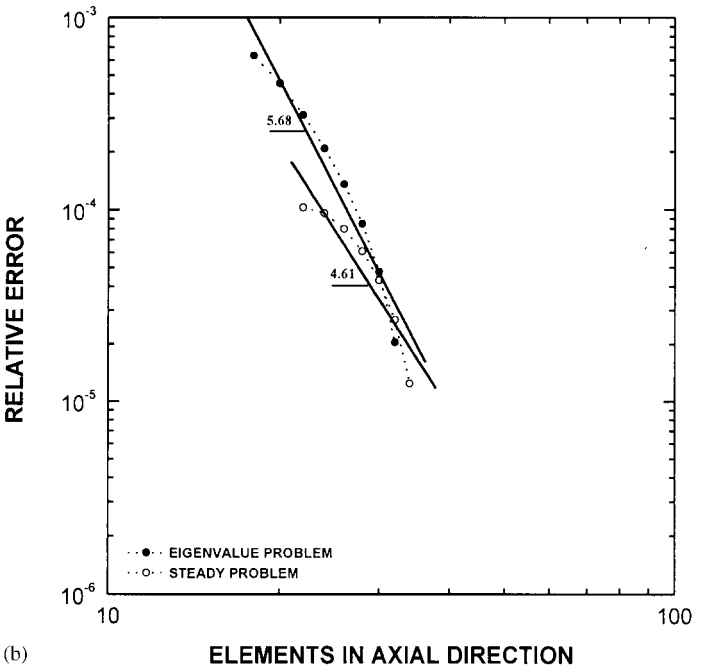


(b)

Figure 8. Variation of the relative error with respect to the number of (a) radial elements for 26 axial and (b) axial elements for six radial elements; PFFEM, for $(\alpha, \Lambda, \beta, V, \mu, \rho, Re, W) = (0.55, \pi/2, 0, 0.7988, 0.05, 1, 7.5, 0.05)$.

Copyright © 2002 John Wiley & Sons, Ltd. 

and 7 is that for both the steady and the eigenvalue problem, the error corresponding to different resolutions oscillates around the thicker line, which has been computed using least squares, in contrast to the results presented in Figures 2 and 3. Comparing now the slopes of Figures 2(a), (2(b)) and Figures 3(a), (3(b)) with those of Figures 6(a), (6(b)) and Figures 7(a), (7(b)), it can be seen that the error decreases more rapidly in the former case than in the latter, although the convergence of the solution remains exponential. In the case of PFFEM (Figures 8(a) and (b)), the relative error for a given mesh is an order of magnitude higher compared to that in Figures 4(a) and (b), a result which indicates that the flow field in the former case is more involved. The convergence rates seem to be quite higher for the steady problem compared to the theoretically predicted ones, while those corresponding to the eigenvalue problem are slightly higher than the asymptotic ones. By setting a relative error to order $10^{-4}$, we compute again the required number of unknowns for each numerical scheme. More specifically, the number of unknowns which are found to be adequate for resolving both the steady solution and the most unstable disturbance are 703, 1046 and 1490 for the SVFSM, PFSM and PFFEM, respectively. Compared with the PFFEM, the decrease in the total number of unknowns is now only 30 per cent for the PFSM and 50 per cent for the SVFSM, while the computation of the same number of eigenvalues using the PFSM and PFFEM formulations requires 2.2 and 4.5 times more computational time than the SVFSM. It is worth pointing out that spurious eigenvalues with positive real parts, (i.e., unstable ones), have been encountered during the previous eigenvalue calculations, irrespective of the formulation or the numerical scheme of solution. These eigenvalues do not disappear with mesh refinement; actually, their growth rates increase and their temporal frequencies persist. Moreover, the corresponding eigenvectors exhibit a node by node spatial oscillation.

Figures 9(a) and (b) show the contour lines of the streamfunction and the periodic part of the pressure for $Re = 7.5$ and for nonzero values of the geometric parameter $\beta$ ($\beta = 0.5$ and 0.9999, respectively). This parameter is varied in order not only to check the ability of the spectral formulations, SVFSM and PFSM, to represent the solution when the geometry of the solid wall approaches a singularity, but also to investigate how the convergence rates of the spectral and the finite element method are affected. When $\beta = 0.9999$, a cusp point is formed on the boundary. It is evident that, even for the larger value of $\beta = 0.9999$, the truncated Fourier series of each variable with bounded variation in the neighborhood of a point of discontinuity does not exhibit the characteristic oscillatory behavior, i.e., the Gibbs phenomenon. This is due to the fact that the discontinuity arises in the derivative but not in the function itself. Comparing the steady streamlines as well as the shapes of solid wall shown in Figure 9, we conclude that the increase of the geometric parameter $\beta$ towards unity makes the radius of the tube wall more uniform, except for the mid-plane, where the singularity is intensified. At the same time, the region where the recirculation of the annular fluid takes place moves towards the cusp as the geometric parameter, $\beta$, increases in size.

In Figures 10 and 11, we examine how the singularity of the solid wall affects the convergence rate of the SVFSM and PFFEM formulations for $Re = 7.5$ and $\beta = 0.9999$. It can be seen in Figure 10(a) that the error decreases exponentially with the number of modes used in the radial direction, and algebraically with the number of modes in the axial direction. Obviously, the convergence rate of the solution with respect to the Fourier modes has been seriously deteriorated since the SVFSM formulation now exhibits just a 2nd order convergence rate. This convergence rate increases after employing considerably more Fourier modes than before. The PFFEM numerical scheme of solution continues to exhibit a nearly

Copyright © 2002 John Wiley & Sons, Ltd. 

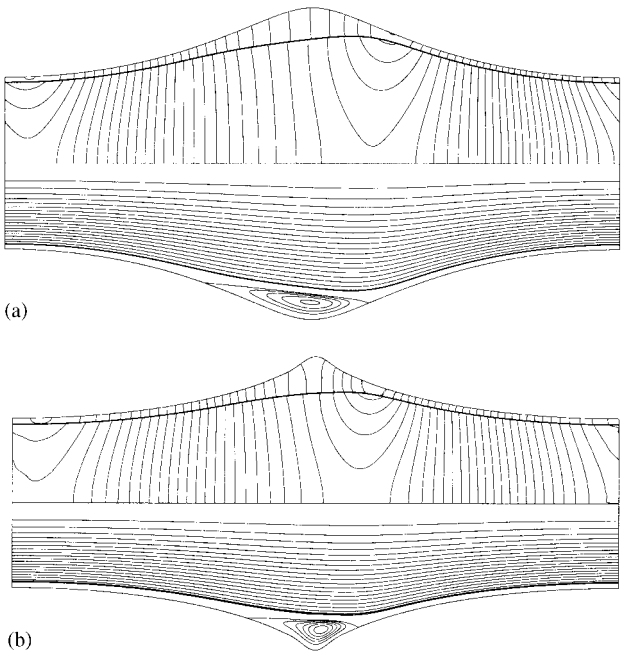


Figure 9. Contour lines of both the pressure (upper half) and the streamfunction (lower half) of the steady solution corresponding to (a) $\beta = 0.5$ and (b) $\beta = 0.9999$, for $(\alpha, \Lambda, V, \mu, \rho, Re, W) = (0.55, \pi/2, 0.7988, 0.05, 1, 7.5, 0.05)$.

4th order convergence rate, as in the previously examined cases, in spite of the singularity in the geometry. Assuming now a relative error of $10^{-3}$, we can compute the required number of unknowns needed for each formulation. More specifically, the SVFSM requires 1785 unknowns, while the PFFEM requires 1276 unknowns. Clearly, the PFFEM handles the singular geometry much more efficiently than the SVFSM scheme, since the latter requires 30 per cent more unknowns and produces a dense matrix. In the PFFEM formulation, there is always a representative node at the axial location of the cusp point, whether even or odd number of elements in the axial direction is used. We have always used an even number of elements in order to map the cusp point onto an inter-element node, where the derivatives of the basis functions are discontinuous, thus handling more efficiently the geometric discontinuity. If an odd number of elements had been used, the cusp region would have been mapped onto an extremely distorted element. The specific choice of collocation points with the pseudo-spectral methods, which is unrelated to the cusp location, prevents them from accurately resolving the flow field near the singularity.

### *6b. Comparison of the methods in dynamic calculations*

In order to validate the PFSM algorithm for even non-axisymmetric disturbances and subsequently to compute the most dangerous eigenvalues in a tube of fairly small constriction ratio, we repeat the eigenvalue calculations reported by Hu and Joseph [27] for core-annular flow in a straight tube. These authors report the unstable eigenvalues for the following three sets

Copyright © 2002 John Wiley & Sons, Ltd. 

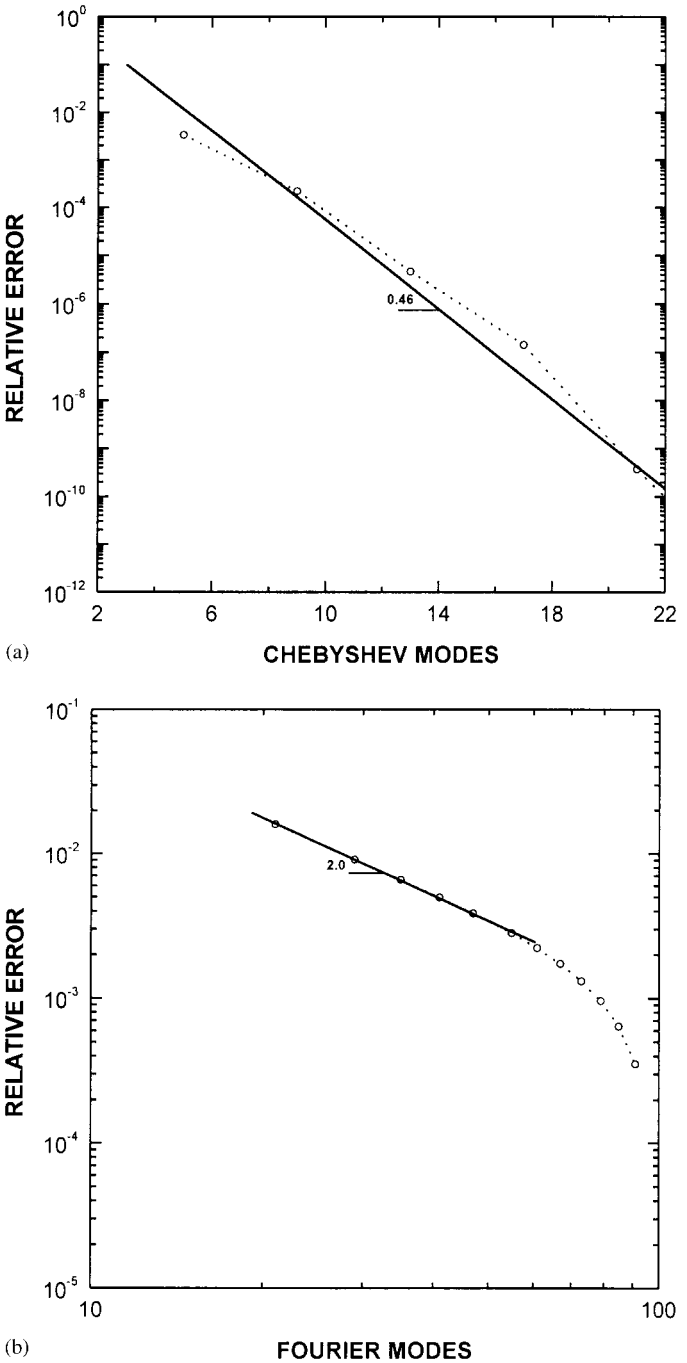


Figure 10. Variation of the relative error of the steady solution with respect to the (a) Chebyshev modes for 31 Fourier modes and (b) Fourier modes for nine Chebyshev modes; SVFSM, for $(\alpha, \Lambda, V, \mu, \rho, Re, W) = (0.55, \pi/2, 0.7988, 0.05, 1, 7.5, 0.05)$.

Copyright © 2002 John Wiley & Sons, Ltd. 

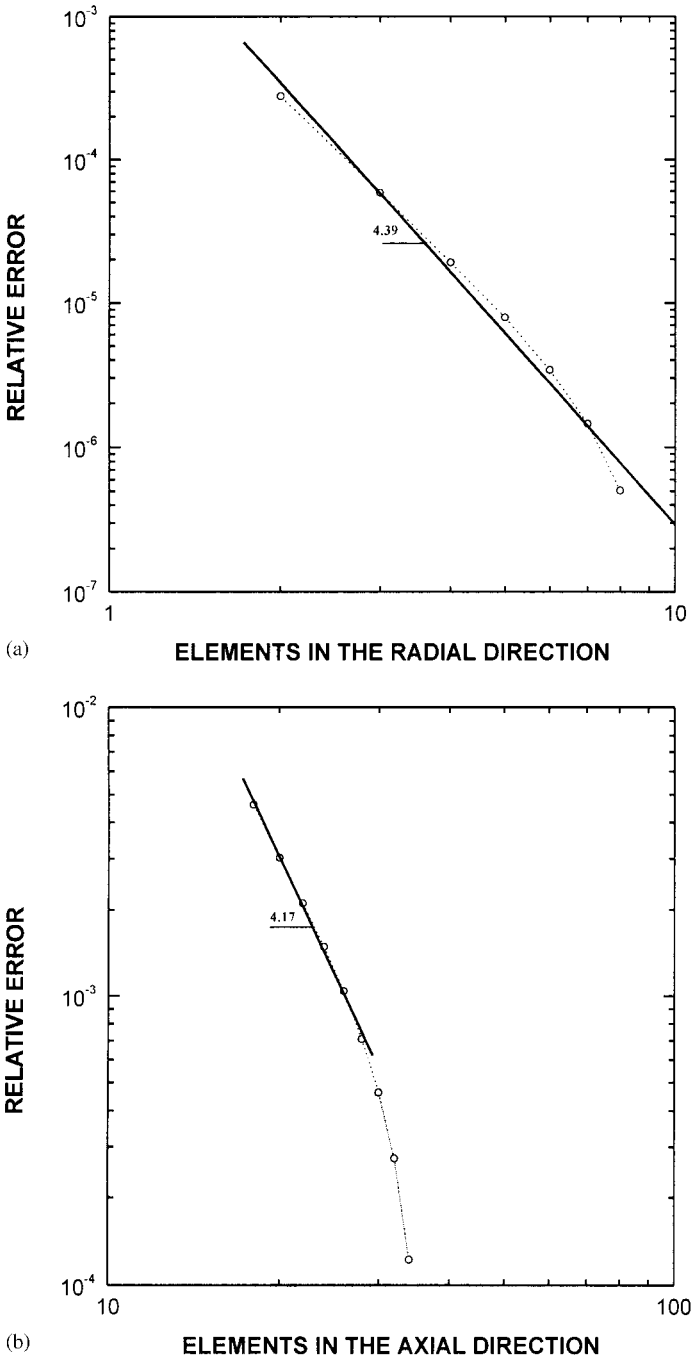


Figure 11. Variation of the relative error of the steady solution with respect to the number of (a) radial elements for 26 axial elements and (b) axial elements for six radial elements; PFFEM, for $(\alpha, \Lambda, V, \mu, \rho, Re, W) = (0.55, \pi/2, 0.7988, 0.05, 1, 7.5, 0.05)$.

Copyright © 2002 John Wiley & Sons, Ltd. 

Table I. Comparison with the results reported by Hu and Joseph [27] for CAF in a straight tube.

| Case | Hu and Joseph [27] | This work (PFSM) | This work (SVFSM) |
|---|---|---|---|
| 1 | $0.020874 \pm 0.38614\,\mathrm{i}$ | $0.020971 \pm 0.38486 \cdot \mathrm{i}$ | $0.020978 \pm 0.38485 \cdot \mathrm{i}$ |
| 2 | $0.004137 \pm 0.66934 \cdot \mathrm{i}$ | $0.004146 \pm 0.66939 \cdot \mathrm{i}$ | $0.004147 \pm 0.66939 \cdot \mathrm{i}$ |
| 3 | $0.003270 \pm 0.67274 \cdot \mathrm{i}$ | $0.003275 \pm 0.67284 \cdot \mathrm{i}$ | — |

Table II. Eigenvalues for an axisymmetric and a non-axisymmetric disturbance.

| $V_1/V_T$ | $k=0$ | $k=1$ | $k=2$ |
|---|---|---|---|
| 0.634 | $0.2048 \times 10^{-1} \pm 0.3902 \times 10^{1} \cdot \mathrm{i}$ | $-0.8463 \times 10^{-1} \pm 0.3838 \times 10^{1} \cdot \mathrm{i}$ | $-0.5895 \times 10^{-1} \pm 0.3978 \times 10^{1} \cdot \mathrm{i}$ |
| 0.259 | $0.1853 \times 10^{-1} \pm 0.3299 \times 10^{1} \cdot \mathrm{i}$ | $-0.7168 \times 10^{-1} \pm 0.3242 \times 10^{1} \cdot \mathrm{i}$ | $-0.5814 \times 10^{0} \pm 0.3360 \times 10^{1} \cdot \mathrm{i}$ |
| 0.207 | $0.3253 \times 10^{-1} \pm 0.3294 \times 10^{1} \cdot \mathrm{i}$ | $-0.9570 \times 10^{-1} \pm 0.3794 \times 10^{1} \cdot \mathrm{i}$ | $-0.1059 \times 10^{1} \pm 0.3950 \times 10^{1} \cdot \mathrm{i}$ |

of values of the parameters $(J^*, \eta, m, \zeta, k, \beta, R^{HJ})$: Case 1: (1000, 0.9, 0.05, 1, 0, 5, 500); Case 2: (0, 0.7, 0.5, 1, 0, 10, 37.78); and Case 3: (0, 0.7, 0.5, 1, 5, 10, 37.78). Their dimensionless numbers are related to ours as follows:

$$\mu = m, \quad \rho = \zeta, \quad \frac{V_1}{V_T} = \eta^2, \quad \Lambda = \beta, \quad A = 1 - m(1-\eta^2)$$
$$Re = \frac{R^{HJ}\beta}{4A}(\eta^4(1-m) + 2(1-\eta^2) - (1+2A\eta^2)) \tag{33}$$
$$W = J^* \left( \frac{4A}{R^{HJ}(\eta^4(1-m) + 2(1-\eta^2) - (1-2A\eta^2))} \right)^2$$

In Table I, we compare the finite element results by Hu and Joseph [27] given in their Table I, for both axisymmetric and non-axisymmetric modes with the eigenvalues we computed using the PFSM and the SVFSM formulations. Since the first two cases correspond to axisymmetric modes, they are studied using both formulations. The third case corresponds to a non-axisymmetric mode with azimuthal wavenumber $k = 5$; hence, the SVFSM formulation cannot be used.

We observe that our calculations are in very good agreement with those of Hu and Joseph [27], which validates our method for non-axisymmetric eigenvalue calculations and the PFSM scheme. Moreover, the results obtained at constant total pressure loss (PFSM) are the same, within computational accuracy, as those obtained at constant volumetric flow rate (SVFSM).

We have performed additional simulations with $(\mu, \rho, Re, W, F, \Lambda, \alpha, N) = (1, 1, 1, 1, 0, 1, 0.75, 1)$, and varied the ratio of the volume of the core fluid to the total volume of the tube, as seen in Table II. The reason for changing only the volume ratio is that studies with a straight tube have shown that decreasing the volume ratio, i.e., the thickness of the core fluid, allows the growth rate of a non-axisymmetric mode to overtake the growth rate of the axisymmetric one [28]. However, this does not happen in our case. Indeed, as shown in Table II, although parameter values have been chosen so that an axisymmetric mode is unstable, all the non-axisymmetric ones remain stable. Table II also demonstrates the stabilizing effect

Copyright © 2002 John Wiley & Sons, Ltd. 

Table III. Most dangerous eigenvalues of the steady solution corresponding to:$(\alpha, \Lambda, \beta, V, \mu, \rho, Re, W) = (0.55, \pi/2, 0, 0.7988, 0.05, 1, 3, 0.5)$.

| One cell ($k=0$) | One cell ($k=1$) | One cell ($k=2$) | Two cells ($k=0$) |
|---|---|---|---|
| $0.06051 \pm 1.5027\cdot i$ | $-0.09100 \pm 1.3737\cdot i$ | $-0.12200 \pm 1.4749\cdot i$ | $0.02454 \pm 0.6866\cdot i$ |
| — | $-0.08607 \pm 3.5372\cdot i$ | $-0.16272 \pm 3.7105\cdot i$ | $0.06051 \pm 1.5027\cdot i$ |
| — | $-0.32584 \pm 6.2778\cdot i$ | $-0.42515 \pm 6.4866\cdot i$ | $0.05549 \pm 2.4907\cdot i$ |

of surface tension on non-axisymmetric modes: as the mode number, $k$, in the azimuthal direction is increased, the real part of the corresponding eigenvalue is reduced.

In Table III, we present the eigenvalues of the linearized equations of motion of the two fluids for the steady solution corresponding to: $(\alpha, \Lambda, \beta, V, \mu, \rho, Re, W) = (0.55, \pi/2, 0, 0.7988, 0.05, 1, 3, 0.5)$. In this case, we have computed the axisymmetric and the first and second non-axisymmetric disturbances, and, in addition, we have doubled the number of the unit cells that comprise the tube by imposing periodicity between the left end of the first cell and the right end of the second one. Apparently, when the tube is composed of two unit cells, the steady flow field is not affected. However, in addition to the unstable eigenvalues that correspond to one cell, there exist others, which do not appear in the one-cell tube, due to the shorter length of the computational domain. Table III also demonstrates the stabilizing effect of surface tension on non-axisymmetric modes, since the real part of the corresponding eigenvalue decreases with the azimuthal wave number, $k$.

Consequently, we can argue that, under the present parameter values, the most unstable eigenvalue arises even if the tube is composed of one unit cell only, and that mode is axisymmetric. Therefore, integrating in time the axisymmetric Navier–Stokes equations in a tube composed of only one unit is accurate, since it will capture the fastest growing disturbance.

The time integration with the previous dimensionless numbers is performed employing the SVFSM and the PFFEM numerical schemes using in all cases as initial condition the steady solution slightly perturbed by including the most unstable eigenvector. It has already been mentioned that even though the time integration with the SVFSM does not produce any spurious results, it is performed incorporating a filtering technique. This is done in order to assess the effect of the filter on the time evolution of the two-phase flow. This effect is measured by comparing the growth rate and the temporal frequency, when the system is very close to the steady solution (i.e., at the initial stages of time integration) with that predicted by the linear theory. Figure 12(a) shows the time evolution of the core flow rate using 11 Chebyshev modes in each phase and 41 Fourier modes in the radial and axial directions, respectively in which case the total number of unknowns equals 1815. Focusing on the region near $t=0$, we observe that the perturbation from the steady solution is indeed very small, i.e., linear: the core flow rate is disturbed from its steady-state value by less than 0.2 per cent. Clearly, no incubation period is required for the instability to set in, since apart from the temporal oscillation the original disturbance grows immediately.

The thick solid line that joins the maxima of the temporal oscillation of the core flow rate is used in order to fit an exponential function with respect to time for time less than 55, shown as the dashed line in Figure 12(a). The computed exponent that results from this fitting is found to be 0.0601, while the temporal frequency computed using Figure 12(a) is found to be 1.500. Clearly, the replication of the linear stability results (see Table III) using dynamic

Copyright © 2002 John Wiley & Sons, Ltd. 

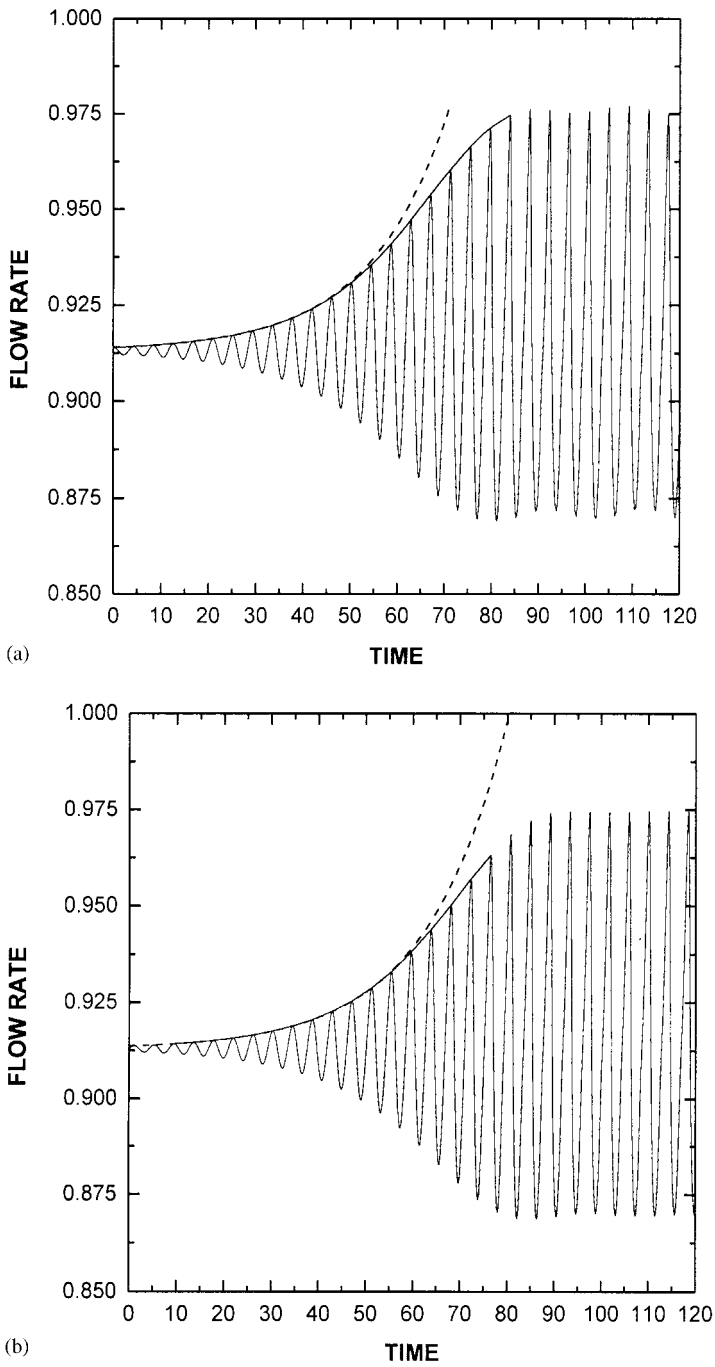


Figure 12. Time evolution of the core flow rate using (a) SVFSM and (b) PFFEM with $(\alpha, \Lambda, \beta, V, \mu, \rho, Re, W) = (0.55, \pi/2, 0, 0.7988, 0.05, 1, 3, 0.5)$.

Copyright © 2002 John Wiley & Sons, Ltd. 

calculations is very good, as we attain accuracy to the third digit for both the growth rate and the frequency of oscillation. Consequently, the effect of the filter is insignificant. This result is not totally unexpected; if we take into account that when the total number of modes is adequate to resolve the flow field, then their further increase does not contribute to the dynamics, since their amplitudes tend to zero almost exponentially, as it happens in this case. As a result, the explicit imposition of these modes to zero has no effect on the time evolution of the two-phase flow. An additional comment that should be made on the time evolution of the core flow rate presented in Figure 12(a) is that, when the instability saturates, the temporal oscillation of the flow rate is not symmetric around the horizontal line representing the flow rate of the steady solution, i.e., 0.9134. This result, which indicates that higher temporal harmonics are introduced due to nonlinear effects, may be responsible for an increased core flow rate compared to the steady solution. In order to examine whether this indeed occurs, we computed the time averaged core flow rate at the entrance of the tube after saturation of the instability (from $t = 100$ to 119.87) and found it to equal 0.913, which is very close to the steady core flow rate. These two findings lead to the requirement that the time variation of the core flow rate must be sharper in its crests than its troughs, something that is also apparent in Figure 12(a). In Figure 12(b) the dynamic response of the core flow rate using the PFFEM scheme is shown. It is obtained using six radial elements in each phase and 30 axial elements, which results in 3668 degrees of freedom. The computed temporal oscillation frequency and growth rates equal 1.503 and 0.0596, which is again very close to the corresponding values computed using linear theory, see Table III.

Figure 13 shows different snapshots of the flow field obtained using the SVFSM numerical scheme. Figure 13(a) shows the flow field that corresponds to the steady solution, while Figures 13(b)–(f) presents the flow field when the instability has saturated and the system has reached a stable limit cycle. More specifically, Figures 13(b)–(f) correspond to times $t = 117.3, 118.15, 119.0$ and 119.85 and 120.5, respectively. The non-linear oscillation period is found to be 4.25 and as a result, Figures 13(b)–(f) correspond to times within one temporal period. The spatially averaged core flow rates computed at the same time instances are found to be 0.9304, 0.9101, 0.8959, 0.9072 and 0.9192, respectively. The sequence of Figures 13(b)–(f) clearly shows that the saturated travelling wave is deforming as it travels downstream. Indeed, as the crest is moving from left to right in the tube and before crossing the mid-plane of the tube, it becomes steeper and its amplitude increases, while after crossing the mid-plane of the tube, it exhibits the opposite behavior. The contour lines of the streamfunction seen in Figures 13(b)–(f) do not change considerably within one temporal period, and their shapes compare well with those of the steady flow, despite the large deviation of the time dependent interface from the steady solution.

## 7. CONCLUSIONS

We have examined the performance of both the spectral and the finite element methods in the study of the core-annular flow in an undulating tube. We have shown that the efficiency of each one of the examined numerical schemes of solution, SVFSM, PFSM and PFFEM, depends on the Reynolds number and the geometry of the solid wall. More specifically, we have shown that when $Re$ is small ($Re = 1$) and the solid wall is a sinusoidal function of the axial distance, the spectral expansions of the variables using either the SVFSM or the

Copyright © 2002 John Wiley & Sons, Ltd. 

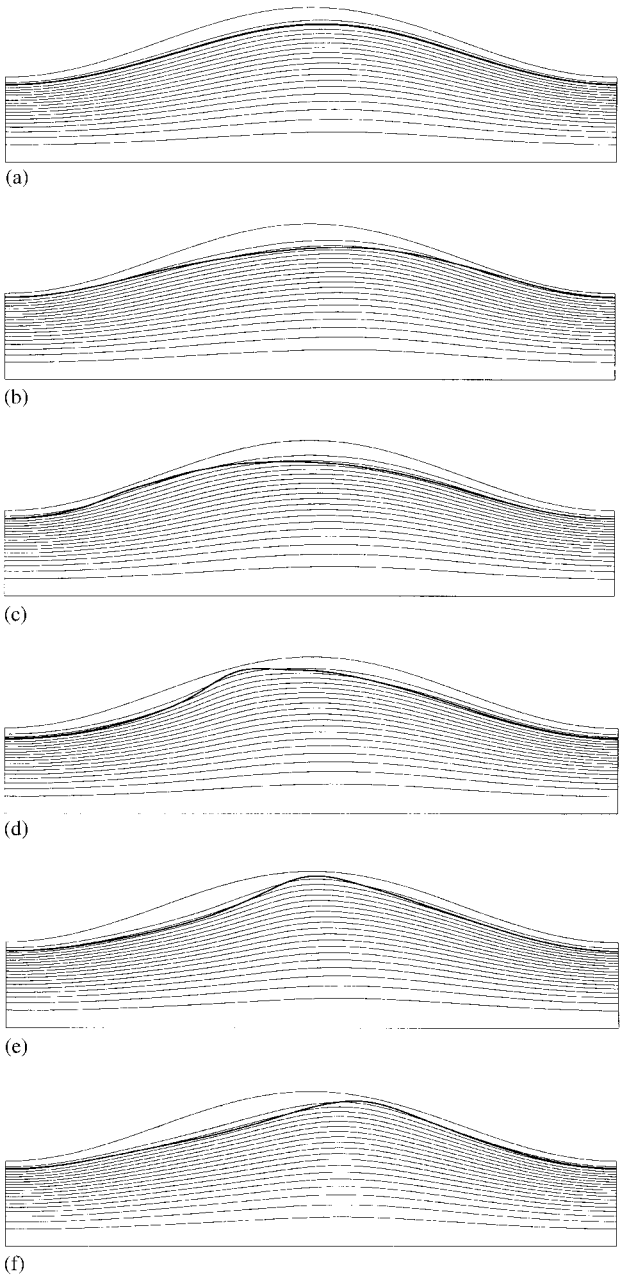


Figure 13. Snapshots of the flow field that correspond to (a) the steady solution, long after the saturation of the instability within one temporal period: (b) $t = 117.3$; (c) $t = 118.15$; (d) $t = 119.0$; (e) $t = 119.85$ and (f) $t = 102.5$ for $(\alpha, \Lambda, \beta, V, \mu, \rho, Re, W) = (0.55, \pi/2, 0, 0.7988, 0.05, 1, 3, 0.5)$.

Copyright © 2002 John Wiley & Sons, Ltd. 

PFSM method lead to a fully coupled system of non-linear equations, and exhibit a clear exponential convergence with the number of unknowns. On the other hand, the PFFEM exhibits approximately a 4th order convergence rate for the steady problem and a 5th or 6th order convergence for the most unstable eigenvalue. The number of unknowns required by each of the numerical schemes, SVFSM, PFSM and PFFEM, equals 377, 715 and 2568, respectively, for a relative error of $10^{-4}$. Apparently, there is great benefit when using the SVFSM scheme, as it involves the least number of unknowns for this case. We have also shown that although the velocity field appears to be symmetric around the mid-plane of the tube, the periodic part of the pressure field is not. This is due to the non-negligible inertia of both fluids in conjunction with the small value of the constriction ratio, which make both fluids accelerate on entering the tube and decelerate in its expanding portion, giving rise in this way to an asymmetry. In addition to the effect of the inertial terms, the capillary forces, which depend on both the Weber number and the curvature of the fluid/fluid interface, intensify further this asymmetry.

Turning to the case with the larger value of $Re$ ($Re = 7.5$), we find that the convergence rates using the PFFEM do not deteriorate, instead they are somewhat accelerated, at least for the steady state calculations. The convergence rates of the SVFSM and the PFSM remain exponential, but the relative error becomes oscillatory. The number of unknowns required by SVFSM, PFSM and PFFEM for similar resolution of both the steady and the eigenvalue problem is found to be 703, 1046 and 1490, respectively. Although the SVFSM scheme still involves the least number of unknowns, the fact that the convergence rate of the PFFEM has been accelerated while that of the SVFSM and PFSM has been slightly reduced results in a reduction in the computational savings of using the pseudo-spectral method compared to that of the finite element method. It is also worth noting that the increase of the relative magnitude of the inertial terms results in the creation of a recirculating region exclusively in the annular fluid domain which is located at the expanding portion of the tube.

We have also examined the ability of each of the above formulations to handle singular geometries. In that case, we have shown that the convergence rate of the SVFSM deteriorates considerably, for meshes similar to those previously used, the method exhibits almost 2nd order convergence rate in the axial direction, while for a finer mesh the convergence rate with respect to the used Fourier modes is accelerated. As in the previous cases, the PFFEM exhibits approximately 4th order convergence rate. The required number of unknowns by the SVFSM and PFFEM for the steady problem is found to be 1785 and 1276, respectively. The latter formulation is by far more efficient, given also that the Jacobian matrix is sparse.

The PFSM numerical scheme of computing axisymmetric and non-axisymmetric eigenvalues has been validated against already reported results concerning the straight tube geometry. The axisymmetric set of equations that govern the motion of both fluids as well as the fluid/fluid interface have been integrated in time using both the PFFEM and the SVFSM formulations. The two formulations reproduce the linear growth rate and the temporal period corresponding to the most unstable mode of the linear stability theory. The above-mentioned formulations, which exhibit the same accuracy, involve 1815 and 3668 unknowns, respectively. The effect of the numerical filter on the dynamics of the CAF is negligible, as it does not introduce damping to the time evolution of the CAF. The computed saturated travelling wave shown in Figures 13(b)–(e) deforms as it travels downstream. In these figures, we also observe that the

Copyright © 2002 John Wiley & Sons, Ltd. 

contour lines of the streamfunction do not change considerably within one temporal period and their shapes are similar to those of the steady flow.

ACKNOWLEDGEMENTS

This work was partially supported under the EKBAN program (Grant number 88, starting year 1998) of the General Secretariat of Research and Technology of Greece and under the EPEAEK program (Grand number 51) of the Ministry of Education of Greece.

REFERENCES

1. Kouris Ch, Neophytides St, Vayenas, CG, Tsamopoulos J. Unsteady state operation of catalytic particles with constant and periodically changing degree of external wetting. *Chemical Engineering Science* 1998; **53**(17):3129–3142.
2. de Santos JM, Melli TR, Scriven LE. Mechanics of gas–liquid flow in packed bed contactors. *Annual Review in Fluid Mechanics* 1991; **23**:233–260.
3. Deiber JA, Schowalter WR. Flow through tubes with sinusoidal axial variations in diameter. *A.I.Ch.E. Journal* 1979; **25**(4):638–645.
4. Lahbabi A, Chang H-C. Flow in periodically constricted tubes: transition to inertial and nonsteady flows. *Chemical Engineering Science* 1986; **41**(10):2487–2505.
5. Pilitsis S, Beris AN. Calculations of steady-state viscoelastic flow in an undulating tube. *Journal of Non-Newtonian Fluid Mechanics* 1989; **31**:231–287.
6. Kouris Ch, Tsamopoulos J. Concentric core-annular flow in a circular tube of slowly varying cross-section. *Chemical Engineering Science* 2000; **55**:5509–5530.
7. Kouris Ch, Tsamopoulos J. Concentric core-annular flow in a periodically constricted tube I. Steady state, energy and linear stability analysis. *Journal of Fluid Mechanics* 2001; **432**:31–68.
8. Hickox CE. Instability due to viscosity and density stratification in axisymmetric pipe flow. *Physics of Fluids* 1971; **14**:251–262.
9. Kerchman V. Strongly nonlinear interfacial dynamics in core-annular flows. *Journal of Fluid Mechanics* 1995; **290**:131–166.
10. Papageorgiou DT, Maldarelli C, Rumschitzki DS. Nonlinear interfacial stability of core-annular film flows. *Physics of Fluids* 1990; **A2**(3):340–352.
11. Li J, Renardy Y. Direct simulation of unsteady axisymmetric core-annular flow with high viscosity ratio. *Journal of Fluid Mechanics* 1999; **391**:123–149.
12. Souvaliotis A, Beris AN. Spectral collocation/domain decomposition method for viscoelastic flow simulations in model porous geometries. *Computer Methods in Applied Mechanics and Engineering* 1996; **129**:9–28.
13. Saez AE, Carbonell RG, Levec J. The hydrodynamics of trickling flow in packed beds Part I: Conduit models. *A.I.Ch.E. Journal* 1986; **32**:353–368.
14. Guzman AM, Amon CH. Dynamical flow characterization of transitional and chaotic regimes in converging–diverging channels. *Journal of Fluid Mechanics* 1996; **321**:25–57.
15. Preziosi L, Chen K, Joseph DD. Lubricated pipelining: stability of core-annular flow. *Journal of Fluid Mechanics* 1989; **201**:323–356.
16. Canuto C, Hussaini MY, Quarteroni A, Zang TA. *Spectral Methods in Fluid Dynamics*. Springer-Verlag: Berlin, 1988.
17. Huyakorn PS, Taylor C, Lee RL, Gresho PM. A comparison of various mixed-interpolation finite elements in the velocity-pressure formulation of the Navier–Stokes equations. *Computers and Fluids* 1978; **6**:25–35.
18. Ruschak KJ. A method for incorporating free boundaries with surface tensions in finite element fluid-flow simulators. *International Journal for Numerical Methods in Engineering* 1980; **15**:639–648.
19. Poslinski AJ, Tsamopoulos JA. Inflation dynamics of fluid annular menisci inside a mold cavity-I. Deformation driven by small gas pressures. *Chemical Engineering Science* 1991; **46**(1):215–232.
20. Lehoucq RB, Scott JA. An evaluation of software for computing eigenvalues of sparse nonsymmetric matrices. *MCS-P547-1195*, *Argonne National Laboratory*, 1996.
21. Sureshkumar R, Beris AN. Linear stability analysis of viscoelastic Poiseuille flow using an Arnoldi-based orthogonalization algorithm. *Journal of Non-Newtonian Fluid Mechanics* 1995; **56**:151–182.
22. Kouris Ch, Tsamopoulos J. Dynamics of axisymmetric core-annular flow I. The more viscous fluid in the core, bamboo waves. *Physics of Fluids* 2001; **13**(4):841–858.
23. Kouris Ch, Tsamopoulos J. Dynamics of axisymmetric core-annular flow II. The less viscous fluid in the core, saw tooth waves. *Physics of Fluids* 2000, submitted for publication.

Copyright © 2002 John Wiley & Sons, Ltd. 

24. Avgousti M, Liu B, Beris AN. Spectral methods for the viscoelastic time-dependent flow equations with applications to Taylor–Couette flow. *International Journal for Numerical Methods in Fluids* 1993; **17**:49–74.
25. Beris AN, Sureshkumar R. Simulation of time-dependent viscoelastic channel Poiseuille flow at high Reynolds numbers. *Chemical Engineering Science* 1996; **51**(9):1451–1471.
26. Osborn J. Approximation of the eigenvalues of a non-selfadjoint operator arising in the study of the stability of stationary solution of the Navier–Stokes equations. *SIAM Journal of Numerical Analysis* 1976; **13**:185–197.
27. Hu HH, Joseph DD. Lubricated pipelining: stability of core-annular flow. Part 2. *Journal of Fluid Mechanics* 1989; **205**:359–396.
28. Hu HH, Patankar N. Non-axisymmetric instability of core-annular flow. *Journal of Fluid Mechanics* 1995; **290**:213–243.

Copyright © 2002 John Wiley & Sons, Ltd. 